

# Global modelling of the early Martian climate under a denser CO<sub>2</sub> atmosphere: Water cycle and ice evolution

R. Wordsworth<sup>a,1</sup> F. Forget<sup>a</sup> E. Millour<sup>a</sup> J. W. Head<sup>b</sup>  
J.-B. Madeleine<sup>a,b</sup> B. Charnay<sup>a</sup>

<sup>a</sup>*Laboratoire de Météorologie Dynamique, Institut Pierre Simon Laplace, Paris, France.*

<sup>b</sup>*Department of Geological Sciences, Brown University, Providence 02912 RI, USA.*

---

## Abstract

We discuss 3D global simulations of the early Martian climate that we have performed assuming a faint young Sun and denser CO<sub>2</sub> atmosphere. We include a self-consistent representation of the water cycle, with atmosphere-surface interactions, atmospheric transport, and the radiative effects of CO<sub>2</sub> and H<sub>2</sub>O gas and clouds taken into account. We find that for atmospheric pressures greater than a fraction of a bar, the adiabatic cooling effect causes temperatures in the southern highland valley network regions to fall significantly below the global average. Long-term climate evolution simulations indicate that in these circumstances, water ice is transported to the highlands from low-lying regions for a wide range of orbital obliquities, regardless of the extent of the Tharsis bulge. In addition, an extended water ice cap forms on the southern pole, approximately corresponding to the location of the Noachian/Hesperian era Dorsa Argentea Formation. Even for a multiple-bar CO<sub>2</sub> atmosphere, conditions are too cold to allow long-term surface liquid water. Limited melting occurs on warm summer days in some locations, but only for surface albedo and thermal inertia conditions that may be unrealistic for water ice. Nonetheless, meteorite impacts and volcanism could potentially cause intense episodic melting under such conditions. Because ice migration to higher altitudes is a robust mechanism for recharging highland water sources after such events, we suggest that this globally sub-zero, ‘icy highlands’ scenario for the late Noachian climate may be sufficient to explain most of the fluvial geology without the need to invoke additional long-term warming mechanisms or an early warm, wet Mars.

*Key words:* Atmospheres, evolution; Mars, atmosphere; Mars, climate; Mars, polar geology; Ices

---

## 1 Introduction

After many decades of observational and theoretical research, the nature of the early Martian climate remains an essentially unsolved problem. Extensive geological evidence indicates that there was both flowing liquid water (e.g., Carr [1995], Irwin et al. [2005], Fassett and Head [2008b], Hynes et al. [2010]) and standing bodies of water (e.g., Fassett and Head [2008b]) on the Martian surface in the late Noachian, but a comprehensive, integrated explanation for the observations remains elusive. As the young Sun was fainter by around 25 % in the Noachian (before approx. 3.5 GYa) [Gough, 1981], to date no climate model has been able to produce long-term warm, wet conditions in this period convincingly. Transient warming events have been proposed to explain some of the observations, but there is still no consensus as to their rate of occurrence or overall importance.

The geomorphological evidence for an altered climate on early Mars includes extensive dendritic channels across the highland Noachian terrain (the famous ‘valley networks’) [Carr, 1996, Fassett and Head, 2008b, Hynes et al., 2010], fossilized river deltas with meandering features [Malin and Edgett, 2003, Fassett and Head, 2005], records of quasi-periodic sediment deposition [Lewis et al., 2008], and regions of enhanced erosion most readily explained through fluvial activity [Hynes and Phillips, 2001]. Some studies have also suggested evidence for an ancient ocean in the low-lying northern plains. These include a global analysis of the martian hydrosphere [Clifford and Parker, 2001] and an assessment of river delta / valley network contact altitudes [di Achille and Hynes, 2010]. However, in the absence of other evidence, the existence of a northern ocean in the Noachian remains highly controversial.

More recent geochemical evidence of aqueous alteration on Mars has both broadened and complicated our view of the early climate. Observations by the OMEGA and CRISM instruments on the Mars Express / Mars Reconnaissance Orbiter spacecraft [Poulet et al., 2005, Bibring et al., 2006, Mustard et al., 2008, Ehlmann et al., 2011] showed widespread evidence for phyllosilicate ( $\sim$ clay) and sulphate minerals across the central and southern Noachian terrain. Surface aqueous minerals are rarer in Mars’ northern lowlands, which are mostly covered by younger Hesperian-era lava plains [Head et al., 2002, Salvatore et al., 2010] and outflow channel effluent [Kreslavsky and Head, 2002]. However, phyllosilicates have been detected in some large northern impact craters that penetrated through these later deposits [Carter et al., 2010]. As these impacts were understood to have excavated ancient Noachian terrain from below the lava plains, it seems plausible that aqueous alteration was once

---

<sup>1</sup> Current address: Department of the Geological Sciences, University of Chicago, 60637 IL, USA.

widespread in both hemispheres, on or just beneath the Martian surface.

Evidence from crater counting [Fassett and Head, 2008a, 2011] suggests that valley network formation was active during the Noachian but ended near the Noachian-Hesperian boundary (approx. 3.5 GYa in their analysis). Broadly speaking, this period overlaps with the end of the period when impacts were frequent and the Tharsis rise was still forming. Interestingly, however, crater statistics also suggest that the main period of phyllosilicate formation ended somewhat before the last valley networks were created. Few Late Noachian open-basin lakes [Fassett and Head, 2008b] show evidence of extensive in-situ phyllosilicates on their floors [Goudge et al., 2012] and in those that do, the clays appear to have been transported there from older deposits by way of valley networks [e.g., Ehlmann et al., 2008].

Interpreting the surface conditions necessary to form the observed phyllosilicates on Mars remains a key challenge to understanding the Noachian climate. It is clear that there is substantial diversity in the early Martian mineralogical record, which probably at least partially reflects progressive changes in environmental conditions over time [Bibring et al., 2006, Mustard et al., 2008, Murchie et al., 2009, Andrews-Hanna et al., 2010, Andrews-Hanna and Lewis, 2011]. Nonetheless, the most recent reviews of the available geochemical evidence suggest that the majority of phyllosilicate deposits may have been formed via subsurface hydrothermal alteration [Ehlmann et al., 2011] or episodic processes, as opposed to a long-term, warm wet climate.

While it is likely that Mars once possessed a thicker CO<sub>2</sub> atmosphere than it has today, it is well known that CO<sub>2</sub> gaseous absorption alone cannot produce a greenhouse effect strong enough to allow liquid water on early Mars at any atmospheric pressure [Kasting, 1991]. Various alternative explanations for an early warm, wet climate have been put forward. Two of the most notable are additional absorption by volcanically emitted sulphur dioxide [Halevy et al., 2007], and downward scattering of outgoing infrared radiation by CO<sub>2</sub> clouds [Forget and Pierrehumbert, 1997]. However, both these hypotheses have been criticised as insufficient in later studies [Colaprete and Toon, 2003, Tian et al., 2010]. Sulphur-induced warming is attractive due to the correlation between the timing of Tharsis formation and the valley networks and the abundance of sulphate minerals on the Martian surface. However, Tian et al. [2010] argued that this mechanism would be ineffective on timescales longer than a few months due to the cooling effects of sulphate aerosol formation in the high atmosphere. CO<sub>2</sub> clouds are a robust feature of cold CO<sub>2</sub> atmospheres that have already been observed in the mesosphere of present-day Mars [Montmessin et al., 2007]. They can cause extremely effective warming via infrared scattering if they form at an optimal altitude and have global coverage close to 100 %. However, our 3D simulations of dry CO<sub>2</sub> atmospheres [Forget et al., 2012] suggest that their warming effect is unlikely to be strong enough to raise

global mean temperatures above the melting point of water for reasonable atmospheric pressures.

Given the problems with steady-state warm, wet models, other researchers have proposed that extreme events such as meteorite impacts could be capable of causing enough warming to explain the observed erosion alone [Segura et al., 2002, 2008, Toon et al., 2010]. These authors proposed that transient steam atmospheres would form for up to several millenia as a result of impacts between 30 and 250 km in diameter. They argued that the enhanced precipitation rates under such conditions would be sufficient to carve valley networks similar to those observed on Mars, and hence that a long-term warm climate was not necessary to explain the geological evidence. This hypothesis has been questioned by later studies – for example, landform evolution modelling of the Parana Valles region ( $-20^{\circ}$  N,  $15^{\circ}$  W) [Barnhart et al., 2009] has suggested that the near-absence of crater rim breaches there is indicative of a long-term, semi-arid climate, as opposed to intermittent catastrophic deluges. Other researchers have argued that with realistic values of soil erodability, there is a significant discrepancy (of order  $10^4$ ) between the estimated Noachian erosion rates and the total erosion possible due to post-impact rainfall (Jim Kasting, private communication). Hence impact-generated steam atmospheres alone still appear unable to explain key elements of the geological observations, and the role of impacts in the Noachian hydrological cycle in general remains unclear.

Most previous theoretical studies of the early Martian climate have used one-dimensional, globally averaged models. While such models have the advantage of allowing a simple and rapid assessment of warming for a given atmosphere, they are incapable of addressing the influence of seasonal and topographic temperature variations on the global water cycle. Johnson et al. [2008] examined the impact of sulphur volatiles on climate in a 3D general circulation model (GCM), but they did not include a dynamic water cycle or the radiative effects of clouds or aerosols. To our knowledge, no other study has yet attempted to model the primitive Martian climate in a 3D GCM.

Here we describe a range of three-dimensional simulations we have performed to investigate possible climate scenarios on early Mars. Our approach has been to study only the simplest possible atmospheric compositions, but to treat all physical processes as accurately as possible. We modelled the early Martian climate in 3D under a denser  $\text{CO}_2$  atmosphere with a) dynamical representation of cloud formation and radiative effects ( $\text{CO}_2$  and  $\text{H}_2\text{O}$ ) b) self-consistent, integrated representation of the water cycle and c) accurate parameterisation of dense  $\text{CO}_2$  radiative transfer. We have studied the effects of varying atmospheric pressure, orbital obliquity, surface topography and starting  $\text{H}_2\text{O}$  inventory. In a companion paper [Forget et al., 2012], we describe the climate under dry (pure  $\text{CO}_2$ ) conditions. Here we focus on the water cycle,

including its effects on global climate and long-term surface ice stabilization. Based on our results, we propose a new hypothesis for valley network formation that combines aspects of previous steady-state and transient warming theories.

In Section 2, we describe our climate model, including the radiative transfer and dynamical modules and assumptions on the water cycle and cloud formation. In Section 3, we describe the results. First, 100% relative humidity simulations are analysed and compared with results assuming a dry atmosphere [Forget et al., 2012]. Next, simulations with a self-consistent water cycle and varying assumptions on the initial CO<sub>2</sub> and H<sub>2</sub>O inventories and surface topography are described. Particular emphasis is placed on a) the long-term evolution of the global hydrology towards a steady state and b) local melting due to short-term transient heating events. In Section 4 we discuss our results in the context of constraints from geological observations and atmospheric evolution theory, and assess the probable effects of impacts during a period of higher flux. Finally, we describe what we view as the most likely scenario for valley network formation in the late Noachian and suggest a few directions for future study.

## 2 Method

To produce our results we used the LMD Generic Climate Model, a new climate simulator with generalised radiative transfer and cloud physics that we have developed for a range of planetary applications [Wordsworth et al., 2010b, Selsis et al., 2011, Wordsworth et al., 2011]. The model uses the LMDZ 3D dynamical core [Hourdin et al., 2006], which is based on a finite-difference formulation of the classical primitive equations of meteorology. The numerical scheme is formulated to conserve both potential enstrophy and total angular momentum [Sadourny, 1975].

Scale-selective hyperdiffusion was used in the horizontal plane for stability, and linear damping was applied in the topmost levels to eliminate the artificial reflection of vertically propagating waves. The planetary boundary layer was parameterised using the method of Mellor and Yamada [1982] and Galperin et al. [1988] to calculate turbulent mixing, with the latent heat of H<sub>2</sub>O also taken into account in the surface temperature calculations when surface ice / water was present. As in Wordsworth et al. [2011], a standard roughness coefficient of  $z_0 = 1 \times 10^{-2}$  m was used for both rocky and ice / water surfaces. A spatial resolution of  $32 \times 32 \times 15$  in longitude, latitude and altitude was used for the simulations. This was slightly greater than the  $32 \times 24 \times 15$  used in most simulations in Forget et al. [2012] to allow more accurate representation of the latitudinal transport of water vapour, but still low enough to allow long-term simulation of system evolution in reasonable computation times.

## 2.1 Radiative transfer

Our radiative transfer scheme was similar to that used in previous studies [e.g., Wordsworth et al., 2011]. For a given mixture of atmospheric gases, we computed high resolution spectra over a range of temperatures, pressures and gas mixing ratios using the HITRAN 2008 database [Rothman et al., 2009]. For this study we used a  $6 \times 9 \times 7$  temperature, pressure and H<sub>2</sub>O volume mixing ratio grid with values  $T = \{100, 150, \dots, 350\}$  K,  $p = \{10^{-3}, 10^{-2}, \dots, 10^5\}$  mbar and  $q_{\text{H}_2\text{O}} = \{10^{-7}, 10^{-6}, \dots, 10^{-1}\}$ , respectively. The correlated- $k$  method was used to produce a smaller database of coefficients suitable for fast calculation in a GCM. The model used 32 spectral bands in the longwave and 36 in the shortwave, and sixteen points for the  $g$ -space integration, where  $g$  is the cumulated distribution function of the absorption data for each band. CO<sub>2</sub> collision-induced absorption was included using a parameterisation based on the most recent theoretical and experimental studies [Wordsworth et al., 2010a, Gruszka and Borysow, 1998, Baranov et al., 2004]. H<sub>2</sub>O lines were truncated at  $25 \text{ cm}^{-1}$ , while the H<sub>2</sub>O continuum was included using the CKD model [Clough et al., 1989]. In clear-sky one-dimensional radiative-convective tests (results not shown) the H<sub>2</sub>O continuum was found to cause an increase of less than 1 K in the global mean surface temperatures under early Mars conditions. A two-stream scheme [Toon et al., 1989] was used to account for the radiative effects of aerosols (here, CO<sub>2</sub> and H<sub>2</sub>O clouds) and Rayleigh scattering, as in Wordsworth et al. [2010b]. The hemispheric mean method was used in the infrared, while  $\delta$ -quadrature was used in the visible. Finally, a solar flux of  $441.1 \text{ W m}^{-2}$  was used (75% of the present-day value), corresponding to the reduced luminosity 3.8 Ga based on standard solar evolution models [Gough, 1981]. For a discussion of the uncertainties regarding the evolution of solar luminosity with time, see Forget et al. [2012].

## 2.2 Water cycle and CO<sub>2</sub> clouds

Three tracer species were used in the simulations: CO<sub>2</sub> ice, H<sub>2</sub>O ice and H<sub>2</sub>O vapour. Tracers were advected in the atmosphere, mixed by turbulence and convection, and subjected to changes due to sublimation / evaporation and condensation and interaction with the surface. For both gases, condensation was assumed to occur when the atmospheric temperature dropped below the saturation temperature. Local mean CO<sub>2</sub> and H<sub>2</sub>O cloud particle sizes were determined from the amount of condensed material and the number density of cloud condensation nuclei [CCN]. The latter parameter was taken to be constant everywhere in the atmosphere. Its effect on cloud radiative effects and hence on climate is discussed in detail in Forget et al. [2012]; here it was

taken to be a global constant for CO<sub>2</sub> clouds (10<sup>5</sup> kg<sup>-1</sup>; see Table 1).

Ice particles of both species were sedimented according to a version of Stokes' law appropriate for a wide range of pressures [Rossow, 1978]. Below the stratosphere, adjustment was used to relax temperatures due to convection and / or condensation of CO<sub>2</sub> and H<sub>2</sub>O. For H<sub>2</sub>O, moist and large-scale convection were taken into account following Manabe and Wetherald [1967]. Precipitation of H<sub>2</sub>O was parameterized using a simple cloud water content threshold  $l_0$  [Emanuel and Ivkovi-Rothman, 1999], with precipitation evaporation also taken into account. Tests using the generic model applied to the present-day Earth showed that this scheme with the value of  $l_0$  given in Table 1 reasonably reproduced the observed cloud radiative effects there. To test the sensitivity of our results to the H<sub>2</sub>O cloud assumptions, we performed a range of simulations where we varied the assumed value of  $l_0$  and  $[CCN]$  for H<sub>2</sub>O clouds. The results of these tests are described in Section 3.2.

On the surface, the local albedo was varied according to the composition (rocky, ocean, CO<sub>2</sub> or H<sub>2</sub>O ice; see Table 1). When the surface ice amount  $q_{ice}$  was lower than a threshold value  $q_{covered} = 33 \text{ kg m}^{-2}$  (corresponding to a uniform layer of approx. 3.5 cm thickness; Le Treut and Li [1991]), partial coverage was assumed and the albedo  $A_s$  was calculated from the rock and water ice albedos  $A_r$  and  $A_i$  as

$$A_s(\theta, \lambda) = A_r + (A_i - A_r) \frac{q_{ice}}{q_{covered}} \quad (1)$$

where  $\theta$  is longitude and  $\lambda$  is latitude. For  $q_{ice} > q_{covered}$ , the local albedo was set to  $A_i$ . When CO<sub>2</sub> ice formed, the local albedo was set to  $A_i$  immediately, as in Forget et al. [2012]. Water ice formation (melting) was assumed to occur when the surface temperature was lower (higher) than 273 K, and the effects of the latent heat of fusion on temperature were taken into account. As in most simulations only transient melting occurred in localised regions, the effects of runoff were not taken into account. Surface temperatures were computed from radiative, sensible and latent surface heat fluxes using an 18-level model of thermal diffusion in the soil [Forget et al., 1999] and assuming a homogeneous thermal inertia (250 J m<sup>-2</sup> s<sup>-1/2</sup> K<sup>-1</sup>). The dependence of the results on the assumption of constant thermal inertia are discussed in Section 3.

### 2.3 Ice equilibration algorithm

The time taken for an atmosphere to reach thermal equilibrium can be estimated from the radiative relaxation timescale [Goody and Yung, 1989]

$$\tau_r = \frac{c_p p_s}{\sigma g T_e^3}, \quad (2)$$

where  $c_p$ ,  $p_s$ ,  $g$ ,  $T_e$  and  $\sigma$  are the specific heat capacity of the atmosphere, the mean surface pressure, the surface gravity, the atmospheric emission temperature and the Stefan-Boltzmann constant, respectively. Taking  $T_e = 200$  K,  $c_p = 800$  J K<sup>-1</sup> kg<sup>-1</sup>,  $p_s = 1$  bar and  $g = 3.72$  m s<sup>-2</sup> yields  $\tau_r \sim 1$  Mars year. For simulations without a water cycle, this was a good approximation to the equilibration time for the entire climate.

When a water cycle is present, equilibration times can be far longer. Particularly for cold climates, where sublimation and light snowfall are the dominant forms of water transport, the surface H<sub>2</sub>O distribution can take thousands of years or more to reach a steady state. Running the 3D model took around 5 hours for one simulated Mars year at the chosen resolution, so evaluating climate evolution in the standard mode was prohibitively time-consuming.

To resolve this problem, we implemented an ice iteration scheme. Starting from the initial surface ice distribution, we ran the GCM normally in intervals of two years. In the second year, we evaluated the annual mean ice rate of change  $\langle \partial h_{ice} / \partial t \rangle$  at each gridpoint. This rate was then multiplied by a multiple-year timestep  $\Delta t$  to give the updated surface ice distribution

$$h_{ice}^+ = h_{ice} + \langle \frac{\partial h_{ice}}{\partial t} \rangle \Delta t. \quad (3)$$

In addition, all ice was removed in regions where  $h_{ice}^+$  dropped below zero or ice coverage was seasonal (i.e.  $h_{ice} = 0$  at some point during the year). After redistribution, the amount in each cell was normalised to conserve the total ice mass in the system  $M_{H_2O}$ . The GCM was then run again for two years and the process repeated until a steady state was achieved.

Trial and error showed that correct choice of the timestep  $\Delta t$  was important: when it was too high, the surface ice distribution tended to fluctuate and did not reach a steady state, while when it was too low the simulations took a prohibitively long time to converge. We used a variable timestep to produce the results described here. For the first 5 iterations,  $\Delta t$  was set to 100 years, after which it was reduced to 10 years for the final 15 iterations. This allowed us to access the final state of the climate system after reasonable computation



times without compromising the accuracy of the results.

In all simulations we set the total ice mass  $M_{H_2O} = 4\pi R^2 q_{covered}$ , with  $R$  the planetary radius. This quantity was chosen so that for completely even ice coverage, the thickness would be 3.5 cm: just enough for the entire surface to have the maximum albedo  $A_i$  [see equation (1)]. While the total Martian  $H_2O$  inventory in the Noachian is likely to have been significantly greater than this, such an approach allows us to study the influence of topography and climate on the steady state of the system without using unreasonably long iteration times. It is also conservative, in the sense that a greater total  $H_2O$  inventory would allow more ice to accumulate in cold-trap regions and hence more potential melting due to seasonal variations or transient events (see Sections 3.2.3 and 4). Two types of initial conditions were used: in the first, ice was restricted to altitudes lower than -4 km from the datum ('icy lowlands'), while in the second, ice was restricted to latitudes of magnitude greater than  $80^\circ$  ('icy poles'). Varying the initial conditions in this way allowed us to study the uniqueness of climate equilibria reached using equation (3).

## 2.4 Topography

Techniques such as spherical elastic shell modelling and statistical crater analysis date the formation of the majority of the Tharsis rise to the mid to late Noachian [Phillips et al., 2001, Fassett and Head, 2011]. Here, we performed most simulations with present-day surface topography, but we also investigated the climatic effects of a reduced Tharsis bulge. For these cases, we used the formula

$$\phi_{mod}(\theta, \lambda) = \phi - (\phi + 4000g)\exp[-(\chi/65^\circ)^{4.5}], \quad (4)$$

to convert the present-day geopotential  $\phi$  to  $\phi_{mod}$ , where  $\chi = ([\theta + 100^\circ]^2 + \lambda^2)^{0.5}$  and  $g$  is surface gravity. Figure 1 compares contour plots of the standard topography and that described by equation (4).

## 3 Results

### 3.1 Fixed atmospheric humidity simulations

In Forget et al. [2012], we described the climate of early Mars with a dense, dry (pure  $CO_2$ ) atmosphere. Here we begin by considering the effects of water vapour on surface temperatures. We performed simulations as in the baseline

Table 1  
Standard parameters used in the climate simulations.

Parameter	Values
Solar flux $F_s$ [ $\text{W m}^{-2}$ ]	441.1
Orbital eccentricity $e$	0.0
Obliquity $\phi$ [degrees]	25.0, 45.0
Surface albedo (rocky) $A_r$	0.2
Surface albedo (liquid water) $A_w$	0.07
Surface albedo ( $\text{CO}_2$ / $\text{H}_2\text{O}$ ice) $A_i$	0.5
Surface topography	present-day, no Tharsis
Initial $\text{CO}_2$ partial pressure $p_{\text{CO}_2}$ [bars]	0.008 to 2
Surface roughness coefficient $z_0$ [m]	$1 \times 10^{-2}$
Surf. therm. inertia $\mathcal{I}$ [ $\text{J m}^{-2} \text{s}^{-1/2} \text{K}^{-1}$ ]	250
$\text{H}_2\text{O}$ precipitation threshold $l_0$ [ $\text{kg kg}^{-1}$ ]	0.001
No. of cloud condens. nuclei [ $CCN$ ] [ $\text{kg}^{-1}$ ]	$1 \times 10^5$

cases of Forget et al. [2012] (variable  $\text{CO}_2$  pressure, circular orbit,  $25^\circ$  obliquity, present-day topography) for a) pure  $\text{CO}_2$  atmospheres and b) atmospheres with relative humidity of 1.0 at all altitudes. In these initial simulations, water vapour was only included in the atmospheric radiative transfer, and not treated as a dynamical tracer or used in convective lapse rate calculations. Neglecting water vapour in lapse rate calculations should only create a small positive surface temperature error in cold climates, and the effect of water clouds on climate in our simulations with a full water cycle was small (this is discussed further later). This approach hence allowed us to place an upper bound on the possible greenhouse warming in our calculations, independent of uncertainties in  $\text{H}_2\text{O}$  convection parameterisations.

In Figure 2, global mean and annual maximum/minimum temperatures from simulations with surface pressures ranging from 0.2 to 2 bar are plotted. Comparison with results for clear  $\text{CO}_2$  atmospheres shows the warming effect of  $\text{CO}_2$  clouds (see Fig. 1 of Forget et al. [2012]). As expected, in atmospheres saturated with water vapour the net warming is greater (by a factor of a few Kelvin to  $\sim 20$  K, depending on the surface pressure). Although there are no scenarios where the mean surface temperature exceeds 273 K, annual maximum temperatures are significantly greater than this in all cases. For pressures greater than 2 bar or less than 0.5 bar, permanent  $\text{CO}_2$  ice caps appeared in the simulations, indicating the onset of atmospheric collapse. As discussed in Forget et al. [2012], finding the equilibrium state in such cases would require extremely long iteration times. Between 0.5 and 2 bar, however,  $\text{CO}_2$  surface

ice was seasonal, and the climate hence reached a steady state on a timescale of order  $\tau_r$  (in the absence of a full water cycle).

In Figure 3, annual mean (top row), diurnally averaged annual maximum (seasonal maximum; middle row) and absolute annual maximum (bottom row) surface temperatures in 2D are plotted for atmospheres of 0.008 (left), 0.2 (middle) and 1 (right) bar pressure in the maximally H<sub>2</sub>O-saturated simulations in equilibrium. The diurnal averaging consisted of a running one-day mean over results sampled 8 times per day. The adiabatic cooling effect described in Forget et al. [2012] is clearly apparent in the annual mean temperatures (Figure 3, top row): at 0.008 and 0.2 bar (left and middle) the main temperature difference is between the poles and the equator, while at 1 bar (right) altitude-temperature correlations dominate. With an atmospheric pressure close to that of Earth, the regions of Mars with the most concentrated evidence for flowing liquid water (the southern Noachian highlands) are among the coldest on the planet.

The seasonal and absolute maximum temperatures are partially correlated with altitude even at 0.2 bar (Figure 3, middle column, middle and bottom), with the result that only small regions of the southern highlands are ever warmer than 273 K at that pressure. At 1 bar, seasonal maximum temperatures (Figure 3, right column, middle) are only above 273 K in the northern plains, parts of Arabia Terra and the Hellas and Argyre basins. However, the absolute maximum temperatures exceed 273 K across most of the planet (Figure 3, right column, bottom) except the Tharsis rise and southern pole. This has interesting implications for the transient melting of water ice, as we describe in the next section.

### 3.2 *Simulations with a water cycle*

When the water cycle is treated self-consistently, surface temperatures can differ from those described in the last section due to a) variations in atmospheric water vapour content, b) the radiative effect of water clouds and c) albedo changes due to surface ice and water. We studied the evolution of the surface ice distribution under these conditions using the ice evolution algorithm described in Section 2. We tested the effects of obliquity, the surface topography and the starting ice distribution in the model.

In general terms, ice should tend to accumulate over time in regions where it is most stable; i.e., the coldest parts of the planet. On present-day Mars, the atmospheric influence on the surface energy balance is small, and the annual mean surface temperature is primarily a function of latitude [e.g., Forget et al., 1999]. However, as discussed in the previous section, increased thermal cou-

pling between the atmosphere and the surface at higher pressures in the past [Forget et al., 2012] would have caused a significantly greater correlation between temperature and altitude, suggesting that ice might have accumulated preferentially in highland regions then. In reality, atmospheric dynamics can also play an important role on the H<sub>2</sub>O surface distribution. This can occur through processes such as topographic forcing of precipitation or the creation of global bands of convergence / divergence (c.f. the inter-tropical convergence zone on Earth, e.g. Pierrehumbert [2011]). The complexity of these effects is an important reason why 3D circulation modelling is required for a self-consistent analysis of the primitive Martian water cycle.

### 3.2.1 *Surface ice evolution*

Figures 4-7 show the evolution of the surface H<sub>2</sub>O ice distribution for several simulations with different initial conditions and topography. Snapshots of the ice are given at the start of the 1<sup>st</sup>, 4<sup>th</sup>, 20<sup>th</sup> and 40<sup>th</sup> years of simulation, with the iteration algorithm applied as described in Section 2.3. Simulations were run for a range of pressures; here we focus on results at 0.008, 0.04 and 1 bar only.

Figure 4 shows two simulations with identical climate parameters (1 bar pressure,  $\phi = 25^\circ$ ) but different initial surface distributions of water ice ('icy lowlands' and 'icy poles' for left and right columns, respectively). As can be seen, the two cases evolve towards similar equilibrium states, with ice present at both poles and in the highest-altitude regions across the planet (the Tharsis bulge, Olympus and Elysium Mons and the Noachian terrain around Hellas basin). The presence of significant amounts of ice over the equatorial regions means an increased planetary albedo. As a result of this and the reduced relative humidity due to localisation of surface H<sub>2</sub>O sources, the mean surface temperature in the final year ( $\sim 233$  K) is several degrees below that of the equivalent 100% humidity simulation. Figure 5 shows the longitudinally and yearly averaged surface ice as a function of time and latitude for the same two simulations. The plots indicate that even at the end of the simulation, the ice density around the equator and in the south was still increasing slightly, mainly at the expense of deposits around 40 °S. Analysis of the atmospheric dynamics (see next section) suggested that low relative humidity associated with convergence of the annual mean meridional circulation at mid-latitudes was responsible for this long-term effect.

In Figure 6 (left column), the same results are plotted for a 1 bar,  $\phi = 25^\circ$  case with modified surface topography as described by equation (4). Here evolution is similar to that in the standard cases, except that the correlation between ice deposits and the distribution of Noachian-era valley networks [see e.g. Fassett and Head, 2008b, Hynek et al., 2010] is even clearer because the Tharsis bulge

is absent. When the obliquity is increased, results are also broadly similar (see  $\phi = 45^\circ$  case; right column of Figure 6), except that ice disappears from the northern pole entirely due to the increased insolation there. The effects of obliquity on ice transport has been discussed in the context of the present-day Martian atmosphere by Forget et al. [2006] and Madeleine et al. [2009]. In these dense-atmosphere simulations, the combination of adiabatic heating and increased insolation in the northern plains at high obliquities makes them the warmest regions of the planet, with mean temperatures of  $\sim 235$  K even for latitudes north of  $5^\circ$  N.

As a test of the ice evolution algorithm, we also performed simulations at 0.008 and 0.04 bar pressure (Figure 7). Converging on a solution proved challenging in these cases, as the rate of H<sub>2</sub>O ice transport was extremely slow, and permanent CO<sub>2</sub> ice caps formed at the poles as on present-day Mars. At 0.008 bar, the total atmospheric mass was so low that after several years the simulations approached a seasonally varying CO<sub>2</sub> vapour-pressure equilibrium. At 0.04 bar, however, atmospheric pressure continued to decrease slowly throughout the simulation.

As a result of the large H<sub>2</sub>O ice evolution timescales, the simulations did not reach an exact equilibrium state even after the full 40 years of simulation time. Nonetheless, Figure 7 clearly shows the differences from the 1-bar case: H<sub>2</sub>O ice is present in large quantities at the poles, with a smaller deposit over the Tharsis bulge. Analysis of the long-term ice trends in these cases (not shown) indicated that the southern polar caps were still slowly growing even at the end of the simulations.

The differences in ice migration between the low and high pressure simulation are easily understood through the adiabatic effect described earlier and shown in Figure 3. In all cases, ice tends to migrate towards the coldest regions on the surface. At 0.008 bar (Figure 3, left-hand column), these regions correlate almost exactly with latitude, while at 1 bar (Figure 3, right-hand column), the correlation is primarily altitude-dependent.

### 3.2.2 Atmospheric dynamics and clouds

Although the primary factor in the H<sub>2</sub>O ice distribution is the annual mean surface temperature distribution, the final steady state was modulated by the effects of the global circulation. Figures 8 and 9 show the annual mean horizontal velocity at the 9th vertical level (approx. 500 hPa; left) and the annual and zonal mean vertical velocity  $\omega$  (right) for the final year of the 1-bar simulation with obliquity  $25^\circ$  and  $45^\circ$ , respectively. As can be seen, the annual mean circulation consists of an equatorial westward jet, with a transition to eastward jets above absolute latitudes of  $40^\circ$ . The associated vertical velocities

are asymmetric as a result of the planet’s north/south topographic dichotomy, with intense vertical shear near  $20^\circ\text{N}$  in both cases. Nonetheless, wide regions of downwelling (positive  $\omega$ ) are apparent around  $50^\circ\text{N/S}$ . In analogy with the latitudinal relative humidity variations due to the meridional overturning circulation on Earth, these features explain the tendency of ice to migrate away from mid-latitudes, as apparent from Figures 4-6 (described in the last section).

Figure 10 shows the total precipitation in each season for the same simulation (obliquity  $25^\circ$ ). It highlights the dramatic annual variations in the meteorology. From  $L_s = 0^\circ$  to  $180^\circ$  (top two maps), relatively intense precipitation (snowfall) occurred in the northernmost regions due to the increased surface temperatures there. In contrast, from  $L_s = 180^\circ$  to  $360^\circ$  (bottom two maps) lighter snowfall occurred in the south, particularly in the high Noachian terrain around Hellas basin where the valley network density is greatest.

Figure 11 shows annual mean column amounts (left) and annual and zonal mean mass mixing ratios (right) of cloud condensate ( $\text{CO}_2$  and  $\text{H}_2\text{O}$ ) for the same simulation. As can be seen,  $\text{CO}_2$  clouds form at high altitudes and vary relatively little with latitude.  $\text{H}_2\text{O}$  clouds form much lower in locations that are dependent on the surface water sources. Because of the Martian north-south topographic dichotomy,  $\text{H}_2\text{O}$  cloud content was much greater in the northern hemisphere, where temperatures were typically warmer in the low atmosphere. We found typical  $\text{H}_2\text{O}$  cloud particle sizes of 2-10  $\mu\text{m}$  in our simulations, although these values were dependent on our choice of cloud condensation nuclei parameter [ $CCN$ ] (set to  $10^5 \text{ kg}^{-1}$  for all the main simulations described here; see Section 2 and Table 1).

To assess the radiative impact of the  $\text{H}_2\text{O}$  clouds, we performed some simulations where the  $\text{H}_2\text{O}$  cloud opacity was set to zero after climate equilibrium had been achieved. Because global mean temperatures were low in our simulations even at one bar  $\text{CO}_2$  pressure and the planetary albedo was already substantially modified by higher-altitude  $\text{CO}_2$  clouds, only small changes (less than 5 K) in the climate were observed. As we used a simplified precipitation scheme and assumed that the water clouds had 100% coverage in each horizontal grid cell of the model, we may have somewhat inaccurately represented their radiative effects. However, mean surface temperatures were already well below 273 K in our saturated water vapour simulations of Section 3.1 at the same pressures, so this is unlikely to have qualitatively affected our results. For a detailed discussion of the coverage and microphysics of  $\text{CO}_2$  clouds in the simulations, refer to Forget et al. [2012].

To assess the uncertainties in our  $\text{H}_2\text{O}$  cloud parameterisation further, we also performed some tests where we varied the number of condensation nuclei [ $CCN$ ] for  $\text{H}_2\text{O}$  and the precipitation threshold  $l_0$  (Table 2). In all tests, we

started from the 1 bar,  $\phi = 25^\circ$  simulations in equilibrium and ran the model for 8 Mars years without ice evolution. We found the effects to be modest; across the range of parameters studied, the total variations in mean surface temperature were under 1 K. The dominating influence of high CO<sub>2</sub> clouds on atmospheric radiative transfer at 1 bar pressure was the most likely cause of this low sensitivity.

When the precipitation threshold was removed altogether, H<sub>2</sub>O clouds became much thicker optically, leading to larger climate differences. In these tests, we observed significant transients in surface temperature, with increases to 250-260 K after one to two years before a slow decline to 200-215 K, after which time permanent CO<sub>2</sub> glaciation usually began to occur. This long-term cooling effect was caused by increased reflection of solar radiation by an extremely thick H<sub>2</sub>O cloud layer, as evidenced by the increased cloud condensate column density and planetary albedo values (Table 2). Particle coagulation is a fundamental physical process in water liquid/ice clouds, and the mean atmospheric densities of condensed H<sub>2</sub>O in these simulations appeared extremely unrealistic when compared to e.g., estimated values for the Earth under snowball glaciation conditions [Abbot et al., 2012]. We therefore did not regard these latter tests to be physically robust, and used the threshold scheme for all simulations with a water cycle presented here. Nonetheless, it is clear that further research in this area in future using more sophisticated cloud schemes would be useful.

Table 2

Sensitivity of the results to H<sub>2</sub>O cloud microphysical parameters. From left to right the columns show the prescribed values of  $[CCN]$  and  $l_0$ , and the simulated global annual mean surface temperature, planetary albedo, H<sub>2</sub>O cloud column density, and H<sub>2</sub>O vapour column density after 10 years simulation time. In all tests  $[CCN]$  was kept constant at  $1 \times 10^5$  kg/kg for the CO<sub>2</sub> clouds.

$[CCN]$ [kg/kg]	$l_0$ [kg/kg]	$\bar{T}_s$ [K]	$A_p$	$\bar{q}_{H_2O}$ cond. [kg m <sup>-2</sup> ]	$\bar{q}_{H_2O}$ vap. [kg m <sup>-2</sup> ]
$1 \times 10^4$	0.001	233.2	0.45	$6.5 \times 10^{-4}$	0.069
$1 \times 10^5$	0.001	232.8	0.45	$4.7 \times 10^{-4}$	0.065
$1 \times 10^6$	0.001	233.5	0.45	$5.5 \times 10^{-4}$	0.070
$1 \times 10^5$	0.01	233.2	0.45	$7.2 \times 10^{-4}$	0.068
$1 \times 10^4$	$\infty$	214.0	0.77	11.1	0.044
$1 \times 10^5$	$\infty$	212.5	0.76	6.37	0.036
$1 \times 10^6$	$\infty$	199.8	0.79	1.17	0.056

### 3.2.3 Transient melting

Figure 12 (top) shows a contour plot of the annual maximum surface liquid H<sub>2</sub>O at each gridpoint after 40 years simulation time for the case shown in Figure 4 (1 bar, 25° obliquity). Given the relatively low spatial resolution of our model and the lack of accurate parameterisations for important sub-gridscale processes (slope effects, small-scale convection etc.), these results can only give an approximate guide to local melting under the simulated global climate. Nonetheless, it is clear that liquid water appears transiently in some amounts across the planet. The increased melting in the northern hemisphere can be explained by the higher temperatures there due to the same adiabatic effect responsible for the migration of ice to the southern highlands.

Figure 12 (bottom) shows surface temperature against time for the four locations shown in Figure 15. The dramatic difference in temperatures between the Tharsis bulge (A) and the bottom of Hellas basin (C) is clear, along with the increased seasonal variation away from the equator (C and D). The transient melting occurring at location D (Utopia Planitia) is clear from the peak of surface temperatures at 273 K there between  $L_s \sim 70$  and  $120^\circ$ . Further heating does not occur in this period because some surface H<sub>2</sub>O ice is still present. In Figure 13, the same results are plotted for the  $\phi = 45^\circ$  case. There, the differences in insolation and absence of ice in the north mean that the great majority of melting events occur south of the equator. As can be seen from the surface temperature plot (bottom), conditions at the equator become cold enough for seasonal CO<sub>2</sub> ice deposits to form on the Tharsis bulge (location A; blue line).

It is well known that Mars’ obliquity evolves chaotically, and during the planet’s history, relatively rapid changes in a range from 0 to 70° are likely to have occurred many times [Laskar et al., 2004]. With this in mind, we investigated the effects of decreasing obliquity to zero, but keeping the end-state surface ice distribution of Figure 4. An obliquity of zero maximises insolation at the equator, which might be expected to maximise melting in the valley network region. However, for this case we found that while mean equatorial temperatures were slightly higher, the lack of seasonal variation reduced annual maximum temperatures in most locations. Hence there was a net decrease in the annual maximum surface liquid water (Figure 14).

To test the sensitivity of the amount of transient melting to our assumed parameters, we also performed some simulations where we varied the H<sub>2</sub>O ice surface albedo and thermal inertia. Starting from the 1 bar, 25° obliquity simulation just described, we a) reduced ice albedo from 0.5 to 0.3 and b) increased the surface ice thermal inertia from  $\mathcal{I} = 250$  to  $1000 \text{ J m}^{-2} \text{ s}^{-1/2} \text{ K}^{-1}$  at all soil depths. In both cases all other parameters were kept constant. Figure 16 shows the results for these two tests in terms of the annual maximum surface



liquid water.

Perhaps unsurprisingly, when the ice albedo was reduced melting occurred over a wider range of surface locations, and the total amount of melting in each year slightly increased. As a variety of processes may influence this parameter, including dust transport and volcanic ash emission [e.g., Wilson and Head, 2007, Kerber et al., 2011], this may have interesting implications for future study. However, increasing the surface ice thermal inertia essentially shut down transient melting entirely (Figure 16, right). As this calculation was performed assuming constant thermal inertia with depth, it clearly represents a lower limit on potential melting. Nonetheless, it indicates that surface seasonal (as opposed to basal) melting on early Mars under these conditions would almost certainly be limited to small regions on the edges of ice sheets only. To constrain the values of these parameters better, a more detailed microphysical / surface model that included the effects of sub-gridscale ice deposition, dust and possibly volcanism would be required.

#### *3.2.4 Southern polar ice and the Dorsa Argentea Formation*

In our simulations, we find that under a dense atmosphere, thick ice sheets form over Mars' southern pole. Ice migrates there preferentially from the north because of the same adiabatic cooling effect responsible for deposition over Tharsis and the equatorial highlands. The Dorsa Argentea Formation is an extensive volatile-rich south polar deposit, with an area that may be as great as 2 % of the total Martian surface [Head and Pratt, 2001]. It is believed to have formed in the late Noachian to early Hesperian era [Plaut et al., 1988], when the atmosphere is likely to have still been thicker than it is today. Given that our simulations span a range of CO<sub>2</sub> pressures, it is interesting to compare the results with geological maps of this region.

As an example, Figure 17 shows surface ice in simulations at 1 bar (25 and 45° obliquity) and 0.2 bar (25° obliquity), with a map plotted alongside that shows the extent of the main geological features [Head and Pratt, 2001]. In Figure 17d, yellow and purple represent the Dorsa Argentea Formation lying on top of the ancient heavily cratered terrain (brown) and below the current (Late Amazonian) polar cap (gray and white). As can be seen, there is a south polar H<sub>2</sub>O cap in all cases, although its latitudinal extent is greatest at 1 bar (Figure 17a). At current obliquity and between 0.2 and 1 bar (Figure 17a, c), the accumulation generally covers the area of the Dorsa Argentea Formation, and also extends toward 180 degrees longitude in the 0.2 bar case, a direction that coincides with the southernmost development of valley networks [Fassett and Head, 2008b, Hynek et al., 2010]. Further simulations of ice formation in this region for moderately dense CO<sub>2</sub> atmospheres would be an interesting topic for future research. In particular, it could be interesting to study southern

polar ice evolution using a zoomed grid or mesoscale model, with possible inclusion of modifying effects due to the dust cycle.

## 4 Discussion

In contrast to the ‘warm, wet’ early Mars envisaged in many previous studies, our simulations depict a cold, icy planet where even transient diurnal melting of water in the highlands can only occur under extremely favourable circumstances. As abundant quantities of liquid water clearly did flow on early Mars, other processes besides those included in our model must therefore have been active at the time. Many cold-climate mechanisms for Martian erosion in the Noachian have been put forward previously, including aquifer recharge by hydrothermal convection [Squyres and Kasting, 1994] and flow at sub-zero temperatures by acidic brines [Gaidos and Marion, 2003, Fairén, 2010]. In the following subsections, we focus on three particularly debated processes: heating by impacts, volcanism, and basal melting of ice sheets.

### 4.1 Meteorite impacts

As noted in Section 1, impacts have already been proposed by Segura et al. [2002, 2008] as the primary cause of the valley networks via the formation of transient steam atmospheres. However, one of the key Segura et al. arguments, namely that the rainfall from these atmospheres post-impact is sufficient to reproduce the observed erosion, has been strongly criticized by other authors [Barnhart et al., 2009]. Nonetheless, the numerous impacts that occurred during the Noachian should have caused local melting of surface ice if glaciers were present. Such a mechanism has been suggested to explain fluvial landforms on fresh Martian impact ejecta [Morgan and Head, 2009, Mangold, 2012]. Under the higher atmospheric pressure and greater impactor flux of the Noachian, it could have caused much more extensive fluvial erosion. However, for impact-induced melting to be a viable explanation for the valley networks, some mechanism to preferentially transport water to the southern highlands must be invoked.

In our simulations, under the denser CO<sub>2</sub> atmosphere that would be expected during Tharsis rise formation, ice was deposited and stabilized in the Noachian highland regions due to the adiabatic cooling effect. Under these circumstances, heating due to impacts could cause extensive melting and hence erosion in exactly the regions where the majority of valley networks are observed [Fassett and Head, 2008b, Hynke et al., 2010]. Transient melting would transport water to lower lying regions, but once temperatures again dropped

below the freezing point of water, the slow transport of ice to the highlands via sublimation and snowfall would recommence. As in our simulations that started with ice at low altitudes, the climate system would then return to a state of equilibrium on much longer timescales. Figure 18 shows a schematic of this process.

Although our results provide a possible solution to one of the problems associated with impact-dominated erosion, the impact hypothesis remains controversial in light of some other observations. For example, young, very large impact craters, such as the Amazonian-era Lyot, have few visible effects of regional or global-scale melting Russell and Head [2002]. In addition, it is still unclear whether the long-term precipitation rates in the highlands predicted by our simulations would provide sufficient  $\text{H}_2\text{O}$  deposition to cause the necessary valley network erosion. Further study of hydrology, climate and erosion rates under the extreme conditions expected post-impact are therefore needed to assess the plausibility of this scenario in detail.

#### 4.2 *Volcanism*

Another potential driver of climate in the Noachian that we have neglected in these simulations is volcanism. As well as causing substantial emissions of  $\text{CO}_2$ , late-Noachian volcanic activity may have influenced the climate via emission of sulphur gases ( $\text{SO}_2$  and  $\text{H}_2\text{S}$ ) and pyroclasts (dust/ash particles) [Halevy et al., 2007, Halevy and Head, 2012, Kerber et al., 2012]. One-dimensional radiative-convective studies have estimated the sulphur gases to have a potential warming effect of up to 27-70 K [Postawko and Kuhn, 1986, Tian et al., 2010], while dust is most likely to cause a small (2-10 K) amount of warming, depending on the particle size and vertical distributions [Forget et al., 2012].

As mentioned in the introduction, Tian et al. [2010] argued that the net effect of volcanism should be to cool the early climate, due to the rapid aerosol formation and hence anti-greenhouse effect that could occur after sulphur gas emission. However, their conclusions were based on the results of one-dimensional climate simulations performed without the effects of  $\text{CO}_2$  clouds included. As described in Forget et al. [2012], carbon dioxide clouds have a major impact on the atmospheric radiative budget by raising planetary albedo and increasing downward IR scattering. As sulphur aerosols would generally be expected to form lower in the atmosphere, it is therefore likely that their radiative effects would be substantially different in a model where clouds were also included. In particular, if aerosols formed in regions already covered by thick  $\text{CO}_2$  clouds, they would likely cause a much smaller increase in planetary albedo than if high clouds were absent. Furthermore, sulphate aerosol particles in the  $\text{CO}_2$ -condensing region of an early Martian atmosphere

would be potential condensation nuclei for the formation of the CO<sub>2</sub> ice cloud crystals, which would further influence the distribution of both aerosol and cloud particles. An extension of the work presented here that included the chemistry and radiative effects of sulphur compounds would therefore be an extremely interesting avenue of future research.

### 4.3 *Basal melting*

It has been proposed that at least some Noachian fluvial features could have formed as a result of the basal melting of glaciers or thick snow deposits [Carr, 1983, Carr and Head, 2003]. Geological evidence suggests that throughout much of the Amazonian, the mean annual surface temperatures of Mars have been so cold that basal melting does not occur in ice sheets or glaciers [e.g., Fastook et al., 2008, Head et al., 2010, Fastook et al., 2011]. However, the documented evidence for extensive and well-developed eskers in the Dorsa Argentea Formation indicates that basal melting and wet-based glaciation occurred at the South Pole near the Noachian-Hesperian boundary. Recent glacial accumulation and ice-flow modeling [Fastook et al., 2012] has shown that to produce significant basal melting for typical Noachian-Hesperian geothermal heat fluxes (45-65 mW m<sup>-2</sup>), mean annual south polar atmospheric temperatures of -50 to -75 °C are required (approximately the same range as we find in our 1 bar simulations). If geologically based approaches to constraining south polar Noachian/Hesperian temperatures such as this prove to be robust, this provides further evidence in favour of a cold and relatively dry early Martian climate.

### 4.4 *Conclusions*

Our results have shown that early Mars is unlikely to have been warm and wet if its atmosphere was composed of CO<sub>2</sub> and H<sub>2</sub>O only, even when the effects of CO<sub>2</sub> clouds are taken into account. It is possible that other greenhouse gases or aerosols due to e.g. Tharsis volcanic emissions also played a role in the climate. However, given current constraints on the maximum amount of CO<sub>2</sub> in the primitive atmosphere (e.g., Grott et al. [2011]; see also Forget et al. [2012] for a detailed discussion), it seems improbable that there was any combination of effects powerful enough to produce a steady-state warm, wet Mars at any time from the mid-Noachian onwards. Despite this, in climates where global mean temperatures are below zero there are still effects that can contribute to transient melting and hence erosion. Simulating the water cycle in 3D has shown that even when the planet is in a state of thermal equilibrium, with mean temperatures as low as ~230 K, seasonal and diurnal

warming can cause some localised melting of  $\text{H}_2\text{O}$ , although the amount that can be achieved depends strongly on the assumed surface albedo and thermal inertia.

As the era of Tharsis formation / volcanism (and hence of increased  $\text{CO}_2$  atmospheric pressure) that we have modelled here occurred at a time of elevated meteorite bombardment, impacts will also have repeatedly caused melting of stable ice deposits in the Noachian highlands. Even if post-impact rainfall was relatively short-term, the fact that ice always returned to higher terrain due to the adiabatic cooling effect means that each impact could have created significant amounts of meltwater in the valley network regions. Volcanic activity, particularly that associated with formation of the Tharsis bulge and Hesperian ridged plains [Head et al., 2002], could also have caused discrete warming events in theory, although it remains to be demonstrated how the anti-greenhouse effect due to sulphate aerosol formation could be overcome in this scenario.

Although we believe these simulations have probably captured the main global features of the steady-state Martian climate in the late Noachian, there are clearly a number of other interesting effects that could be investigated in future. We have not included dust or volcanic emissions in our simulations. Both of these are likely to have had an important effect during the Noachian, and adding them in future would allow a more complete assessment of the nature of the early water cycle. Modelling the effects of impacts directly in 3D could also lead to interesting insights, although robust parameterization of many physical processes across wide temperature ranges and short timescales would be necessary to do this accurately. A more immediate application could be to couple the climate model described here with a more detailed subsurface / hydrological scheme. Such an approach could be particularly revealing in localised studies of cases where geothermal processes or residual heating due to impacts may have been important [e.g., Abramov and Kring, 2005]. In future, integration of 3D climate models with specific representations of warming processes (both local and global) should allow a detailed assessment of whether the observed Noachian fluvial features can be reconciled with the cold, mainly frozen planet simulated here.

## Acknowledgements

This article has benefited from discussions with many researchers, including Jim Kasting, Nicolas Mangold, William Ingram, Alan Howard, Bob Haberle and Franck Selsis.

## References

- D. S. Abbot, A. Voigt, M. Branson, R. T. Pierrehumbert, D. Pollard, G. Le Hir, and D. D. B. Koll. Clouds and Snowball Earth Deglaciation. *Geophysical Research Letters*, October 2012.
- O. Abramov and D. A. Kring. Impact-induced hydrothermal activity on early Mars. *Journal of Geophysical Research (Planets)*, 110:E12S09, November 2005. doi: 10.1029/2005JE002453.
- J. C. Andrews-Hanna and K. W. Lewis. Early Mars hydrology: 2. Hydrological evolution in the Noachian and Hesperian epochs. *Journal of Geophysical Research (Planets)*, 116:E02007, February 2011. doi: 10.1029/2010JE003709.
- J. C. Andrews-Hanna, M. T. Zuber, R. E. Arvidson, and S. M. Wiseman. Early Mars hydrology: Meridiani playa deposits and the sedimentary record of Arabia Terra. *Journal of Geophysical Research (Planets)*, 115:E06002, June 2010. doi: 10.1029/2009JE003485.
- Y. I. Baranov, W. J. Lafferty, and G. T. Fraser. Infrared spectrum of the continuum and dimer absorption in the vicinity of the O<sub>2</sub> vibrational fundamental in O<sub>2</sub>/CO<sub>2</sub> mixtures. *Journal of Molecular Spectroscopy*, 228: 432–440, December 2004. doi: 10.1016/j.jms.2004.04.010.
- C. J. Barnhart, A. D. Howard, and J. M. Moore. Long-term precipitation and late-stage valley network formation: Landform simulations of Parana Basin, Mars. *Journal of Geophysical Research (Planets)*, 114:E01003, January 2009. doi: 10.1029/2008JE003122.
- J.-P. Bibring, Y. Langevin, J. F. Mustard, F. Poulet, R. Arvidson, A. Gendrin, B. Gondet, N. Mangold, P. Pinet, and F. Forget. Global Mineralogical and Aqueous Mars History Derived from OMEGA/Mars Express Data. *Science*, 312:400–404, April 2006. doi: 10.1126/science.1122659.
- M. H. Carr. Stability of streams and lakes on Mars. *Icarus*, 56:476–495, December 1983. doi: 10.1016/0019-1035(83)90168-9.
- M. H. Carr. The Martian drainage system and the origin of valley networks and fretted channels. *Journal of Geophysical Research*, 100:7479–7507, April 1995. doi: 10.1029/95JE00260.
- M. H. Carr. *Water on Mars*. New York: Oxford University Press, —c1996, 1996.
- M. H. Carr and J. W. Head. Basal melting of snow on early Mars: A possible origin of some valley networks. *Geophysical Research Letters*, 30(24):2245, December 2003. doi: 10.1029/2003GL018575.
- J. Carter, F. Poulet, J.-P. Bibring, and S. Murchie. Detection of Hydrated Silicates in Crustal Outcrops in the Northern Plains of Mars. *Science*, 328: 1682–, June 2010. doi: 10.1126/science.1189013.
- S. M. Clifford and T. J. Parker. The Evolution of the Martian Hydrosphere: Implications for the Fate of a Primordial Ocean and the Current State of the Northern Plains. *Icarus*, 154:40–79, November 2001. doi: 10.1006/icar.2001.6671.
- S.A. Clough, F.X. Kneizys, and R.W. Davies. Line shape and the water vapor

- continuum. *Atmospheric Research*, 23(3-4):229–241, 1989. ISSN 0169-8095.
- A. Colaprete and O. B. Toon. Carbon dioxide clouds in an early dense Martian atmosphere. *Journal of Geophysical Research (Planets)*, 108:5025, April 2003. doi: 10.1029/2002JE001967.
- G. di Achille and B. M. Hynek. Ancient ocean on Mars supported by global distribution of deltas and valleys. *Nature Geoscience*, 3:459–463, July 2010. doi: 10.1038/ngeo891.
- B. L. Ehlmann, J. F. Mustard, S. L. Murchie, F. Poulet, J. L. Bishop, A. J. Brown, W. M. Calvin, R. N. Clark, D. J. Des Marais, R. E. Milliken, L. H. Roach, T. L. Roush, G. A. Swayze, and J. J. Wray. Orbital Identification of Carbonate-Bearing Rocks on Mars. *Science*, 322:1828–, December 2008. doi: 10.1126/science.1164759.
- B. L. Ehlmann, J. F. Mustard, S. L. Murchie, J.-P. Bibring, A. Meunier, A. A. Fraeman, and Y. Langevin. Subsurface water and clay mineral formation during the early history of Mars. *Nature*, 479:53–60, November 2011. doi: 10.1038/nature10582.
- K. A. Emanuel and M. Ivkovi-Rothman. Development and Evaluation of a Convection Scheme for Use in Climate Models. *Journal of Atmospheric Sciences*, 56:1766–1782, 1999.
- A. G. Fairén. A cold and wet Mars. *Icarus*, 208:165–175, July 2010. doi: 10.1016/j.icarus.2010.01.006.
- C. I. Fassett and J. W. Head. Fluvial sedimentary deposits on Mars: Ancient deltas in a crater lake in the Nili Fossae region. *Geophysical Research Letters*, 32:L14201, July 2005. doi: 10.1029/2005GL023456.
- C. I. Fassett and J. W. Head. The timing of martian valley network activity: Constraints from buffered crater counting. *Icarus*, 195:61–89, May 2008a. doi: 10.1016/j.icarus.2007.12.009.
- C. I. Fassett and J. W. Head. Valley network-fed, open-basin lakes on Mars: Distribution and implications for Noachian surface and subsurface hydrology. *Icarus*, 198:37–56, November 2008b. doi: 10.1016/j.icarus.2008.06.016.
- C. I. Fassett and J. W. Head. Sequence and timing of conditions on early Mars. *Icarus*, 211:1204–1214, February 2011. doi: 10.1016/j.icarus.2010.11.014.
- J. L. Fastook, J. W. Head, D. R. Marchant, and F. Forget. Tropical mountain glaciers on Mars: Altitude-dependence of ice accumulation, accumulation conditions, formation times, glacier dynamics, and implications for planetary spin-axis/orbital history. *Icarus*, 198:305–317, December 2008. doi: 10.1016/j.icarus.2008.08.008.
- J. L. Fastook, J. W. Head, F. Forget, J.-B. Madeleine, and D. R. Marchant. Evidence for Amazonian northern mid-latitude regional glacial landsystems on Mars: Glacial flow models using GCM-driven climate results and comparisons to geological observations. *Icarus*, 216:23–39, November 2011. doi: 10.1016/j.icarus.2011.07.018.
- James L. Fastook, James W. Head, David R. Marchant, Francois Forget, and Jean-Baptiste Madeleine. Early mars climate near the noachianhesperian boundary: Independent evidence for cold conditions from basal melting of

- the south polar ice sheet (dorsa argentea formation) and implications for valley network formation. *Icarus*, 219(1):25 – 40, 2012. ISSN 0019-1035. doi: 10.1016/j.icarus.2012.02.013. URL <http://www.sciencedirect.com/science/article/pii/S0019103512000619>.
- F. Forget and R. T. Pierrehumbert. Warming Early Mars with Carbon Dioxide Clouds That Scatter Infrared Radiation. *Science*, 278:1273–+, November 1997.
- F. Forget, F. Hourdin, R. Fournier, C. Hourdin, O. Talagrand, M. Collins, S. R. Lewis, P. L. Read, and J.-P. Huot. Improved general circulation models of the Martian atmosphere from the surface to above 80 km. *Journal of Geophysical Research*, 104:24155–24176, 1999.
- F. Forget, R. M. Haberle, F. Montmessin, B. Levrard, and J. W. Head. Formation of Glaciers on Mars by Atmospheric Precipitation at High Obliquity. *Science*, 311:368–371, January 2006. doi: 10.1126/science.1120335.
- F. Forget, R. Wordsworth, E. Millour, J.-B. Madeleine, L. Kerber, J. Leconte, E. Marcq, and R. M. Haberle. Global modeling of the early Martian climate under a denser CO<sub>2</sub> atmosphere: Temperature and CO<sub>2</sub> ice clouds. *Submitted to Icarus*, 2012.
- E. Gaidos and G. Marion. Geological and geochemical legacy of a cold early Mars. *Journal of Geophysical Research (Planets)*, 108:5055, June 2003. doi: 10.1029/2002JE002000.
- B. Galperin, L. H. Kantha, S. Hassid, and A. Rosati. A Quasi-equilibrium Turbulent Energy Model for Geophysical Flows. *Journal of Atmospheric Sciences*, 45:55–62, 1988.
- R. M. Goody and Y. L. Yung. *Atmospheric radiation: Theoretical basis*. 1989.
- T. A. Goudge, J. F. Mustard, J. W. Head, and C. I. Fassett. Constraints on the History of Open-Basin Lakes on Mars from the Timing of Volcanic Resurfacing. In *Lunar and Planetary Institute Science Conference Abstracts*, volume 43 of *Lunar and Planetary Institute Science Conference Abstracts*, page 1328, March 2012.
- D. O. Gough. Solar interior structure and luminosity variations. *Solar Physics*, 74:21–34, November 1981.
- M. Grott, A. Morschhauser, D. Breuer, and E. Hauber. Volcanic outgassing of CO<sub>2</sub> and H<sub>2</sub>O on Mars. *Earth and Planetary Science Letters*, 308:391–400, August 2011. doi: 10.1016/j.epsl.2011.06.014.
- M. Gruszka and A. Borysow. Computer simulation of the far infrared collision induced absorption spectra of gaseous CO<sub>2</sub>. *Molecular Physics*, 93:1007–1016, 1998. doi: 10.1080/002689798168709.
- I. Halevy and J. W. Head. Climatic Effects of Punctuated Volcanism on Early Mars. *LPI Contributions*, 1680:7043, May 2012.
- I. Halevy, M. T. Zuber, and D. P. Schrag. A Sulfur Dioxide Climate Feedback on Early Mars. *Science*, 318:1903–, December 2007. doi: 10.1126/science.1147039.
- J. W. Head and S. Pratt. Extensive Hesperian-aged south polar ice sheet on Mars: Evidence for massive melting and retreat, and lateral flow and



- ponding of meltwater. *Journal of Geophysical Research*, 106:12275–12300, June 2001. doi: 10.1029/2000JE001359.
- J. W. Head, M. A. Kreslavsky, and S. Pratt. Northern lowlands of Mars: Evidence for widespread volcanic flooding and tectonic deformation in the Hesperian Period. *Journal of Geophysical Research (Planets)*, 107:5003, January 2002. doi: 10.1029/2000JE001445.
- J. W. Head, D. R. Marchant, J. L. Dickson, A. M. Kress, and D. M. Baker. Northern mid-latitude glaciation in the Late Amazonian period of Mars: Criteria for the recognition of debris-covered glacier and valley glacier landsystem deposits. *Earth and Planetary Science Letters*, 294:306–320, June 2010. doi: 10.1016/j.epsl.2009.06.041.
- F. Hourdin, I. Musat, S. Bony, P. Braconnot, F. Codron, J.-L. Dufresne, L. Fairhead, M.-A. Filiberti, P. Friedlingstein, J.-Y. Grandpeix, G. Krinner, P. Levan, Z.-X. Li, and F. Lott. The LMDZ4 general circulation model: climate performance and sensitivity to parametrized physics with emphasis on tropical convection. *Climate Dynamics*, 27:787–813, December 2006. doi: 10.1007/s00382-006-0158-0.
- B. M. Hynek and R. J. Phillips. Evidence for extensive denudation of the Martian highlands. *Geology*, 29:407–+, May 2001. doi: 10.1130/0091-7613(2001)029<0407:EFEDOT>2.0.CO;2.
- B. M. Hynek, M. Beach, and M. R. T. Hoke. Updated global map of Martian valley networks and implications for climate and hydrologic processes. *Journal of Geophysical Research (Planets)*, 115:E09008, September 2010. doi: 10.1029/2009JE003548.
- R. P. Irwin, A. D. Howard, R. A. Craddock, and J. M. Moore. An intense terminal epoch of widespread fluvial activity on early Mars: 2. Increased runoff and paleolake development. *Journal of Geophysical Research (Planets)*, 110(9):12–+, December 2005. doi: 10.1029/2005JE002460.
- S. S. Johnson, M. A. Mischna, T. L. Grove, and M. T. Zuber. Sulfur-induced greenhouse warming on early Mars. *Journal of Geophysical Research (Planets)*, 113(12):8005–+, August 2008.
- J. F. Kasting. CO<sub>2</sub> condensation and the climate of early Mars. *Icarus*, 94:1–13, November 1991.
- L. Kerber, J. W. Head, J.-B. Madeleine, F. Forget, and L. Wilson. The dispersal of pyroclasts from Apollinaris Patera, Mars: Implications for the origin of the Medusae Fossae Formation. *Icarus*, 216:212–220, November 2011. doi: 10.1016/j.icarus.2011.07.035.
- L. Kerber, F. Forget, J. B. Madeleine, R. Wordsworth, J. W. Head, and L. Wilson. The Effect of Atmospheric Pressure on the Dispersal of Pyroclasts from Martian Volcanoes. In *Lunar and Planetary Institute Science Conference Abstracts*, volume 43 of *Lunar and Planetary Institute Science Conference Abstracts*, page 1295, March 2012.
- M. A. Kreslavsky and J. W. Head. Fate of outflow channel effluents in the northern lowlands of Mars: The Vastitas Borealis Formation as a sublimation residue from frozen ponded bodies of water. *Journal of Geophysical*

- Research (Planets)*, 107:5121, December 2002. doi: 10.1029/2001JE001831.
- J. Laskar, A. C. M. Correia, M. Gastineau, F. Joutel, B. Levrard, and P. Robutel. Long term evolution and chaotic diffusion of the insolation quantities of Mars. *Icarus*, 170:343–364, August 2004. doi: 10.1016/j.icarus.2004.04.005.
- Hervé Le Treut and Zhao-Xin Li. Sensitivity of an atmospheric general circulation model to prescribed sst changes: feedback effects associated with the simulation of cloud optical properties. *Climate Dynamics*, 5:175–187, 1991. ISSN 0930-7575. URL <http://dx.doi.org/10.1007/BF00251808>. 10.1007/BF00251808.
- K. W. Lewis, O. Aharonson, J. P. Grotzinger, R. L. Kirk, A. S. McEwen, and T.-A. Suer. Quasi-Periodic Bedding in the Sedimentary Rock Record of Mars. *Science*, 322:1532–, December 2008. doi: 10.1126/science.1161870.
- J.-B. Madeleine, F. Forget, J. W. Head, B. Levrard, F. Montmessin, and E. Millour. Amazonian northern mid-latitude glaciation on Mars: A proposed climate scenario. *Icarus*, 203:390–405, October 2009. doi: 10.1016/j.icarus.2009.04.037.
- M. C. Malin and K. S. Edgett. Evidence for Persistent Flow and Aqueous Sedimentation on Early Mars. *Science*, 302:1931–1934, 2003.
- S. Manabe and R. T. Wetherald. Thermal Equilibrium of the Atmosphere with a Given Distribution of Relative Humidity. *Journal of Atmospheric Sciences*, 24:241–259, May 1967. doi: 10.1175/1520-0469(1967)024<0241:TEOTAW>2.0.CO;2.
- N. Mangold. Fluvial landforms on fresh impact ejecta on Mars. *Planetary and Space Science*, 62:69–85, March 2012. doi: 10.1016/j.pss.2011.12.009.
- G. L. Mellor and T. Yamada. Development of a Turbulence Closure Model for Geophysical Fluid Problems. *Reviews of Geophysics*, 20:851–875, 1982.
- F. Montmessin, B. Gondet, J.-P. Bibring, Y. Langevin, P. Drossart, F. Forget, and T. Fouchet. Hyperspectral imaging of convective CO<sub>2</sub> ice clouds in the equatorial mesosphere of Mars. *JGR (Planets)*, 112:11–+, November 2007.
- G. A. Morgan and J. W. Head. Sinton crater, Mars: Evidence for impact into a plateau icefield and melting to produce valley networks at the Hesperian-Amazonian boundary. *Icarus*, 202:39–59, July 2009. doi: 10.1016/j.icarus.2009.02.025.
- S. L. Murchie, J. F. Mustard, B. L. Ehlmann, R. E. Milliken, J. L. Bishop, N. K. McKeown, E. Z. Noe Dobrea, F. P. Seelos, D. L. Buczkowski, S. M. Wiseman, R. E. Arvidson, J. J. Wray, G. Swayze, R. N. Clark, D. J. Des Marais, A. S. McEwen, and J.-P. Bibring. A synthesis of Martian aqueous mineralogy after 1 Mars year of observations from the Mars Reconnaissance Orbiter. *Journal of Geophysical Research (Planets)*, 114:E00D06, September 2009. doi: 10.1029/2009JE003342.
- J. F. Mustard, S. L. Murchie, S. M. Pelkey, B. L. Ehlmann, R. E. Milliken, J. A. Grant, J.-P. Bibring, F. Poulet, J. Bishop, E. N. Dobrea, L. Roach, F. Seelos, R. E. Arvidson, S. Wiseman, R. Green, C. Hash, D. Humm, E. Malaret, J. A. McGovern, K. Seelos, T. Clancy, R. Clark, D. D. Marais, N. Izenberg, A. Knudson, Y. Langevin, T. Martin, P. McGuire, R. Morris,

- M. Robinson, T. Roush, M. Smith, G. Swayze, H. Taylor, T. Titus, and M. Wolff. Hydrated silicate minerals on Mars observed by the Mars Reconnaissance Orbiter CRISM instrument. *Nature*, 454:305–309, July 2008. doi: 10.1038/nature07097.
- R. J. Phillips, M. T. Zuber, S. C. Solomon, M. P. Golombek, B. M. Jakosky, W. B. Banerdt, D. E. Smith, R. M. E. Williams, B. M. Hynek, O. Aharonson, and S. A. Hauck. Ancient Geodynamics and Global-Scale Hydrology on Mars. *Science*, 291:2587–2591, March 2001. doi: 10.1126/science.1058701.
- R.T. Pierrehumbert. *Principles of Planetary Climate*. Cambridge University Press, 2011. ISBN 9780521865562. URL [http://books.google.com/books?id=b0\\_U8f5pVR8C](http://books.google.com/books?id=b0_U8f5pVR8C).
- J. J. Plaut, R. Kahn, E. A. Guinness, and R. E. Arvidson. Accumulation of sedimentary debris in the south polar region of Mars and implications for climate history. *Icarus*, 76:357–377, November 1988. doi: 10.1016/0019-1035(88)90076-0.
- S. E. Postawko and W. R. Kuhn. Effect of the greenhouse gases ( $\text{CO}_2$ ,  $\text{H}_2\text{O}$ ,  $\text{SO}_2$ ) on martian paleoclimate. *Journal of Geophysical Research*, 91:431–D438, September 1986.
- F. Poulet, J.-P. Bibring, J. F. Mustard, A. Gendrin, N. Mangold, Y. Langevin, R. E. Arvidson, B. Gondet, and C. Gomez. Phyllosilicates on Mars and implications for early martian climate. *Nature*, 438:623–627, December 2005. doi: 10.1038/nature04274.
- W. B. Rossow. Cloud microphysics - Analysis of the clouds of Earth, Venus, Mars, and Jupiter. *Icarus*, 36:1–50, October 1978. doi: 10.1016/0019-1035(78)90072-6.
- L. S. Rothman, I. E. Gordon, A. Barbe, D. C. Benner, P. F. Bernath, M. Birk, V. Boudon, L. R. Brown, A. Campargue, J.-P. Champion, K. Chance, L. H. Coudert, V. Dana, V. M. Devi, S. Fally, J.-M. Flaud, R. R. Gamache, A. Goldman, D. Jacquemart, I. Kleiner, N. Lacome, W. J. Lafferty, J.-Y. Mandin, S. T. Massie, S. N. Mikhailenko, C. E. Miller, N. Moazzen-Ahmadi, O. V. Naumenko, A. V. Nikitin, J. Orphal, V. I. Perevalov, A. Perrin, A. Predoi-Cross, C. P. Rinsland, M. Rotger, M. Šimečková, M. A. H. Smith, K. Sung, S. A. Tashkun, J. Tennyson, R. A. Toth, A. C. Vandaele, and J. Vander Auwera. The HITRAN 2008 molecular spectroscopic database. *Journal of Quantitative Spectroscopy and Radiative Transfer*, 110:533–572, 2009. doi: 10.1016/j.jqsrt.2009.02.013.
- P. S. Russell and J. W. Head. The martian hydrosphere/cryosphere system: Implications of the absence of hydrologic activity at Lyot crater. *Geophysical Research Letters*, 29(17):1827, September 2002. doi: 10.1029/2002GL015178.
- R. Sadourny. The Dynamics of Finite-Difference Models of the Shallow-Water Equations. *Journal of Atmospheric Sciences*, 32:680–689, 1975.
- M. R. Salvatore, J. F. Mustard, M. B. Wyatt, and S. L. Murchie. Definitive evidence of Hesperian basalt in Acidalia and Chryse planitiae. *Journal of Geophysical Research (Planets)*, 115:E07005, July 2010. doi: 10.1029/

- 2009JE003519.
- T. L. Segura, O. B. Toon, A. Colaprete, and K. Zahnle. Environmental Effects of Large Impacts on Mars. *Science*, 298:1977–1980, December 2002.
- T. L. Segura, O. B. Toon, and A. Colaprete. Modeling the environmental effects of moderate-sized impacts on Mars. *Journal of Geophysical Research (Planets)*, 113:E11007, November 2008. doi: 10.1029/2008JE003147.
- F. Selsis, R. D. Wordsworth, and F. Forget. Thermal phase curves of nontransiting terrestrial exoplanets. I. Characterizing atmospheres. *Astronomy and Astrophysics*, 532:A1+, August 2011. doi: 10.1051/0004-6361/201116654.
- S. W. Squyres and J. F. Kasting. Early Mars: How Warm and How Wet? *Science*, 265:744–749, August 1994. doi: 10.1126/science.265.5173.744.
- F. Tian, M. W. Claire, J. D. Haqq-Misra, M. Smith, D. C. Crisp, D. Catling, K. Zahnle, and J. F. Kasting. Photochemical and climate consequences of sulfur outgassing on early Mars. *Earth and Planetary Science Letters*, 295: 412–418, July 2010. doi: 10.1016/j.epsl.2010.04.016.
- O. B. Toon, C. P. McKay, T. P. Ackerman, and K. Santhanam. Rapid calculation of radiative heating rates and photodissociation rates in inhomogeneous multiple scattering atmospheres. *Journal of Geophysical Research*, 94:16287–16301, November 1989.
- O. B. Toon, T. Segura, and K. Zahnle. The Formation of Martian River Valleys by Impacts. *Annual Review of Earth and Planetary Sciences*, 38: 303–322, May 2010. doi: 10.1146/annurev-earth-040809-152354.
- L. Wilson and J. W. Head. Explosive volcanic eruptions on Mars: Tephra and accretionary lapilli formation, dispersal and recognition in the geologic record. *Journal of Volcanology and Geothermal Research*, 163:83–97, June 2007. doi: 10.1016/j.jvolgeores.2007.03.007.
- R. Wordsworth, F. Forget, and V. Eymet. Infrared collision-induced and far-line absorption in dense CO<sub>2</sub> atmospheres. *Icarus*, 210:992–997, December 2010a. doi: 10.1016/j.icarus.2010.06.010.
- R. Wordsworth, F. Forget, F. Selsis, J.-B. Madeleine, E. Millour, and V. Eymet. Is Gliese 581d habitable? Some constraints from radiative-convective climate modeling. *Astronomy and Astrophysics*, 522:A22+, 2010b. doi: 10.1051/0004-6361/201015053.
- R. D. Wordsworth, F. Forget, F. Selsis, E. Millour, B. Charnay, and J.-B. Madeleine. Gliese 581d is the First Discovered Terrestrial-mass Exoplanet in the Habitable Zone. *The Astrophysical Journal Letters*, 733:L48+, June 2011. doi: 10.1088/2041-8205/733/2/L48.

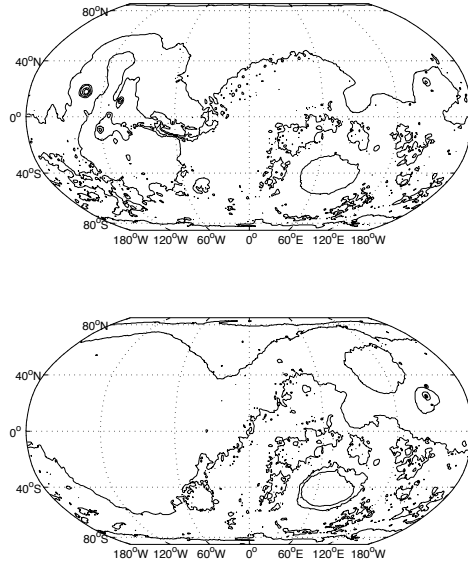


Fig. 1. Comparison of present-day Martian topography (top) with the reduced Tharsis bulge topography (bottom) described by equation (4) and used in some simulations.

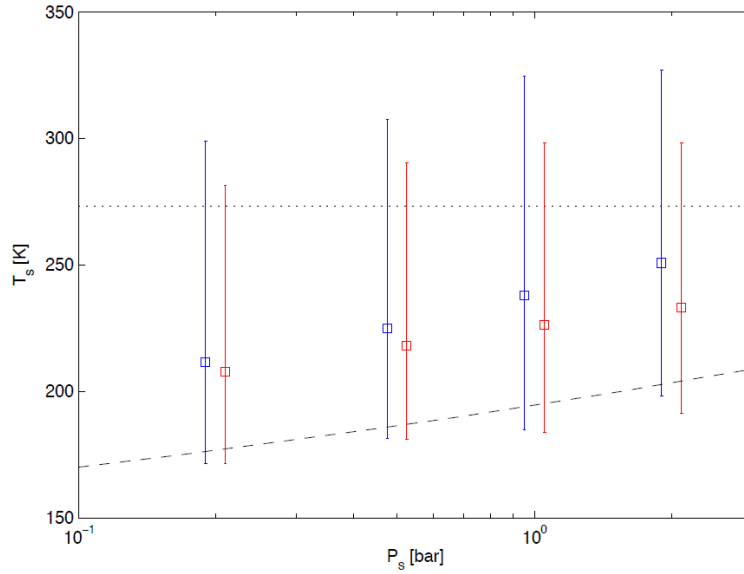


Fig. 2. Effects of atmospheric  $\text{CO}_2$  and  $\text{H}_2\text{O}$  on global temperature. Error bars show mean and maximum / minimum surface temperature vs. pressure (sampled over one orbit and across the surface) for dry  $\text{CO}_2$  atmospheres (red), and simulations with 100% relative humidity (blue) but no  $\text{H}_2\text{O}$  clouds. Dashed and dotted black lines show the condensation curve of  $\text{CO}_2$  and the melting point of  $\text{H}_2\text{O}$ , respectively. For this plot simulations were performed at 0.2, 0.5, 1 and 2 bar; the dry and wet data are slightly separated for clarity only.

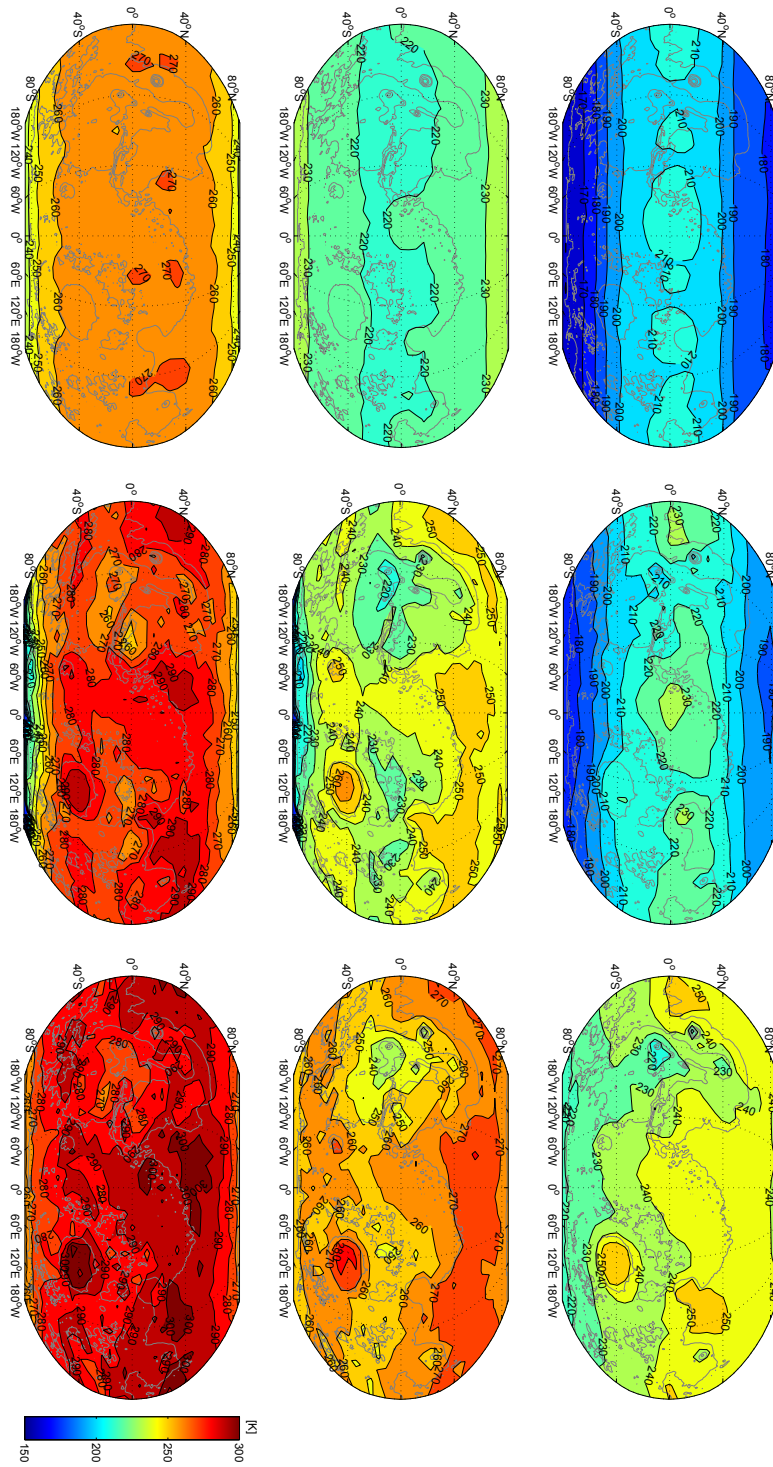


Fig. 3. Surface temperature mean and variations in the 100% relative humidity simulations. Top, middle and bottom plots show the annual mean, the diurnally averaged annual maximum, and the absolute annual maximum, respectively. Left, right and center columns are for 0.008, 0.2 and 1 bar, respectively. Black contours show the topography used in the simulation. Strong correlation of annual mean surface temperature with altitude (as occurs on e.g. present-day Earth and Venus) is apparent in the 0.2 and 1 bar cases.

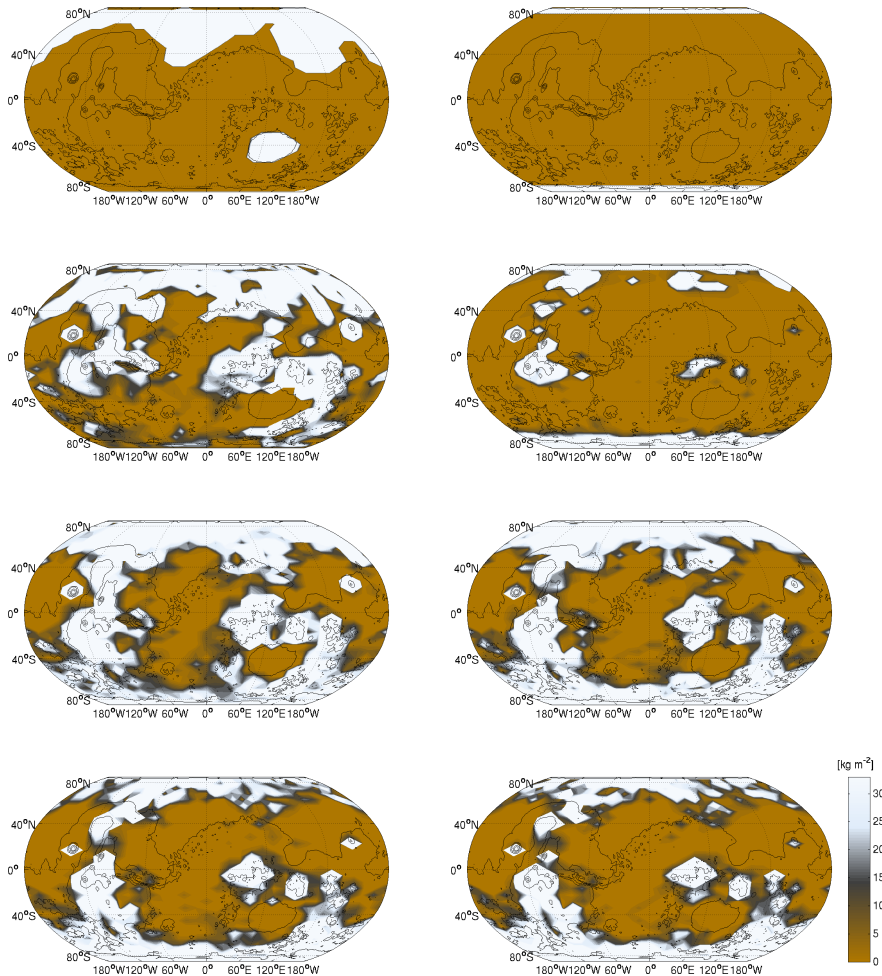


Fig. 4. Evolution of  $\text{H}_2\text{O}$  ice in simulations using the iteration scheme described in Section 2. From top to bottom, plots show surface ice density in  $\text{kg m}^{-2}$  at the start of the simulation and annual mean after 4, 20 and 40 Mars years. Ice iteration was performed every two years, with a 100-year timestep used for the first 5 iterations and 10-year timesteps used thereafter. Simulations were performed at 1 bar mean surface pressure with obliquity  $25^\circ$ . Left and right columns show cases with initial ice deposits in low-lying regions and at the poles, respectively.

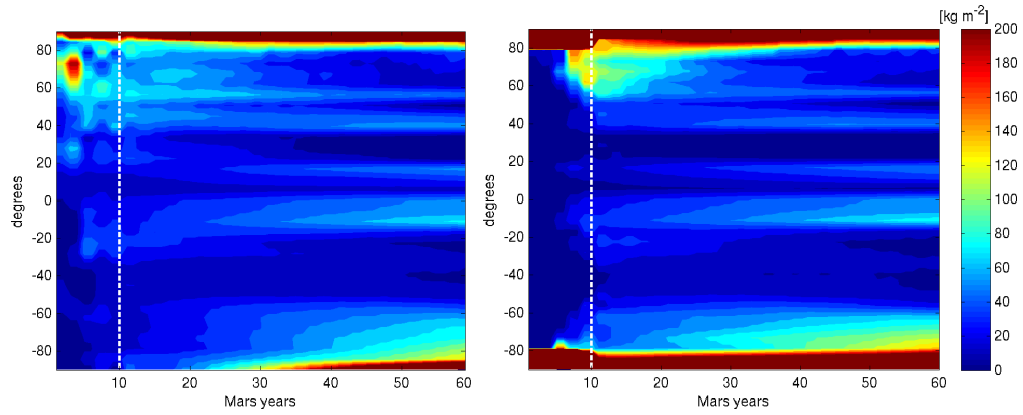


Fig. 5. Zonally and yearly averaged H<sub>2</sub>O surface ice density as a function of latitude and time for the same simulations as in Figure 4. The dotted vertical line indicates the transition from 100-year to 10-year timesteps in the ice evolution algorithm.

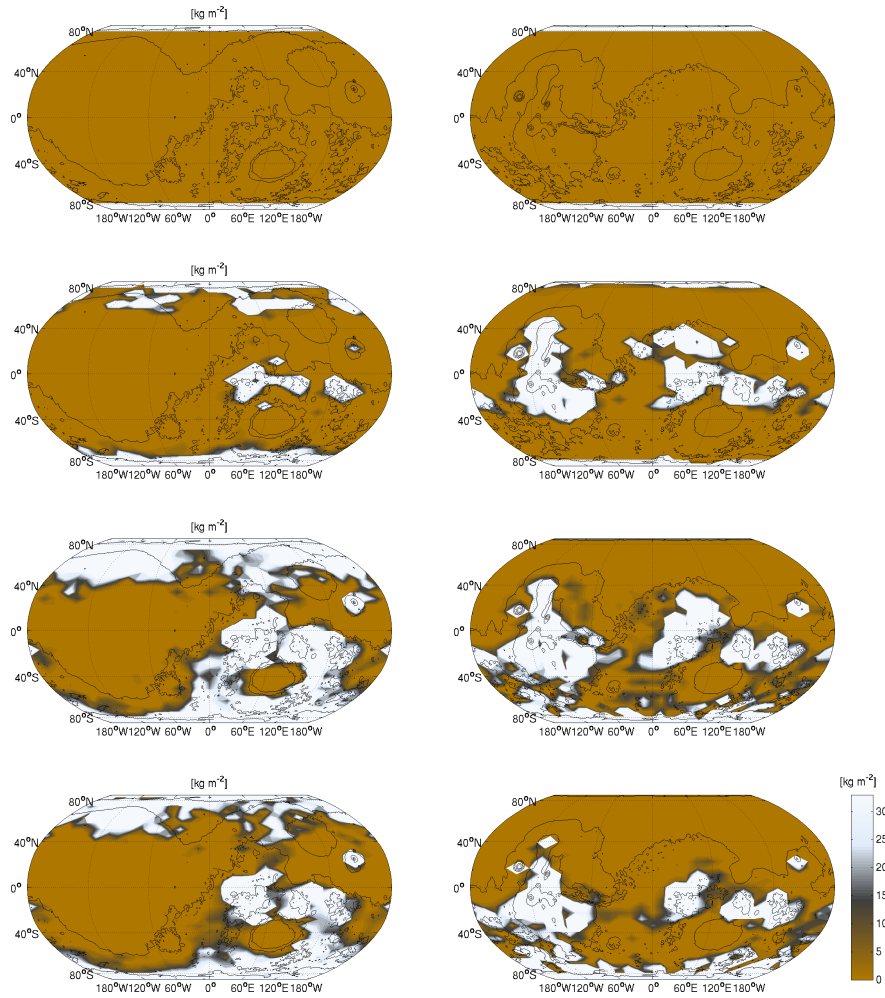


Fig. 6. Same as Figure 4 (right column) except with modified topography (left) and with obliquity increased to 45° (right).



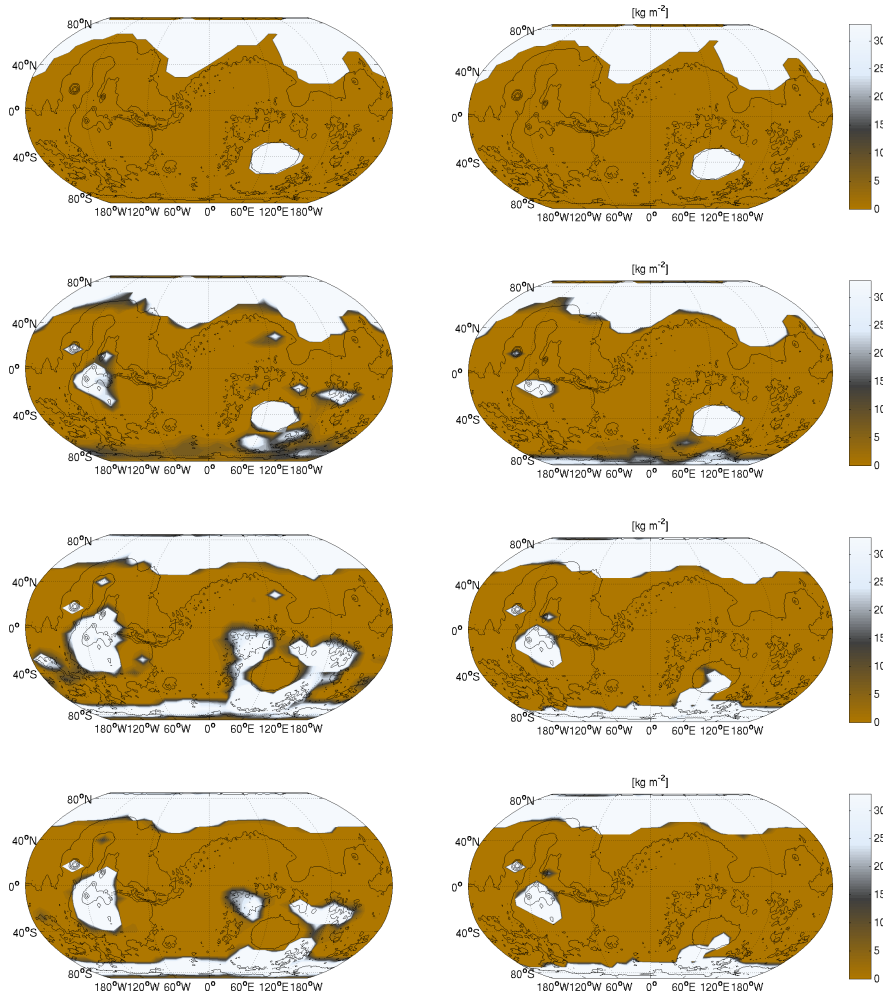


Fig. 7. Same as Figure 4 (left column) except for surface pressure of 0.04 bar (left) and 0.008 bar (right).

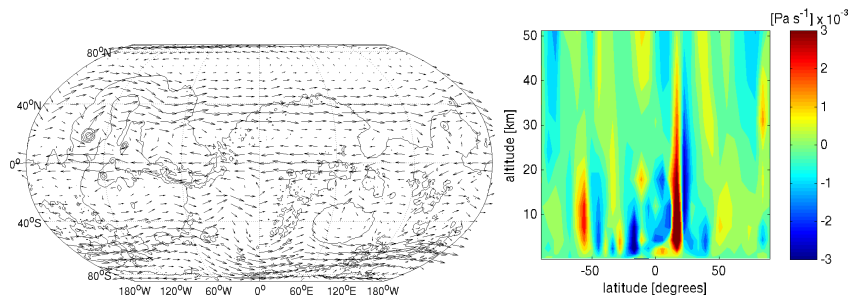


Fig. 8. (left) Annual mean horizontal wind in the middle atmosphere (at approx. 500 hPa) and (right) annual and zonal mean vertical velocity (right), for the 1-bar 25° obliquity case after 40 simulation years.

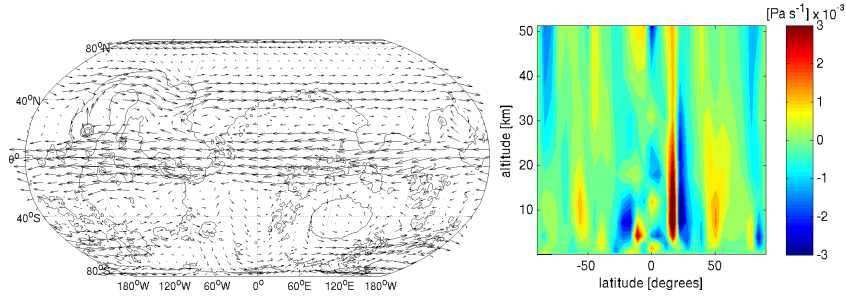


Fig. 9. Same as Figure 8, but for  $45^\circ$  obliquity.

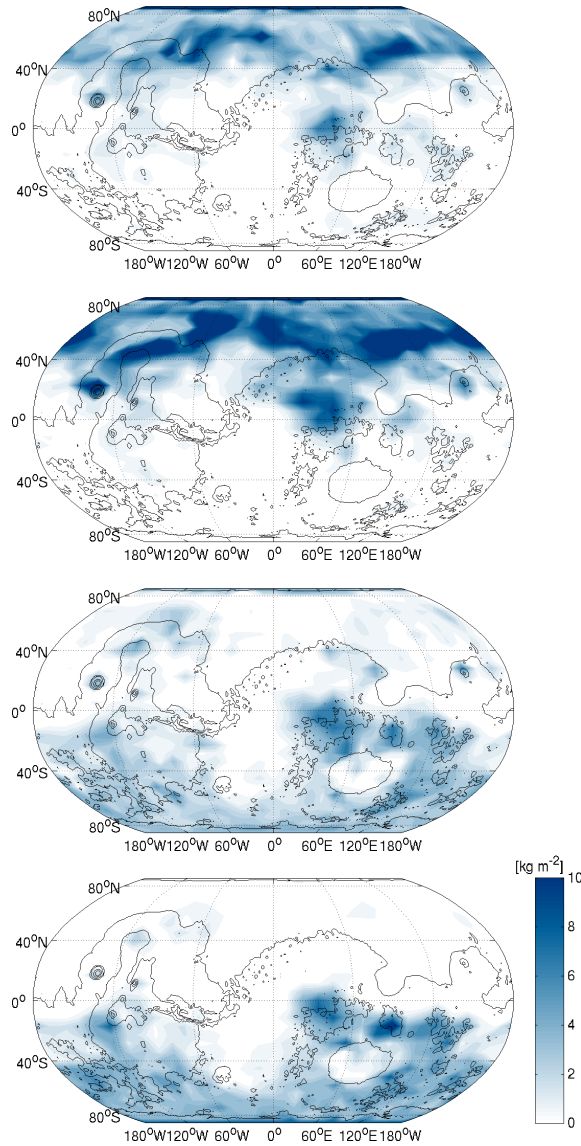


Fig. 10. Total precipitation (snowfall) in each season for  $L_s = 0^\circ$  to  $90^\circ$ ,  $90^\circ$  to  $180^\circ$ ,  $180^\circ$  to  $270^\circ$  and  $270^\circ$  to  $360^\circ$  (in descending order), for the 1-bar  $25^\circ$  obliquity case after 40 simulation years.

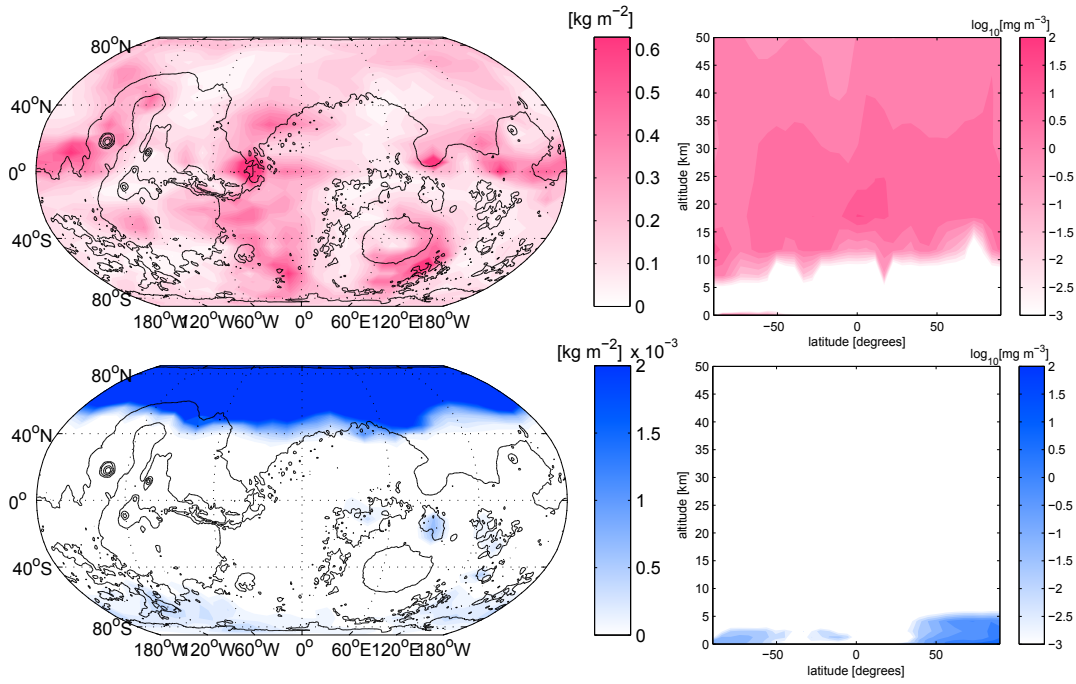


Fig. 11. Annual mean column amounts (left) and annual and zonal mean mass mixing ratios (right) of CO<sub>2</sub> (red) and H<sub>2</sub>O (blue) cloud condensate for the 1-bar 25° obliquity case after 40 simulation years.

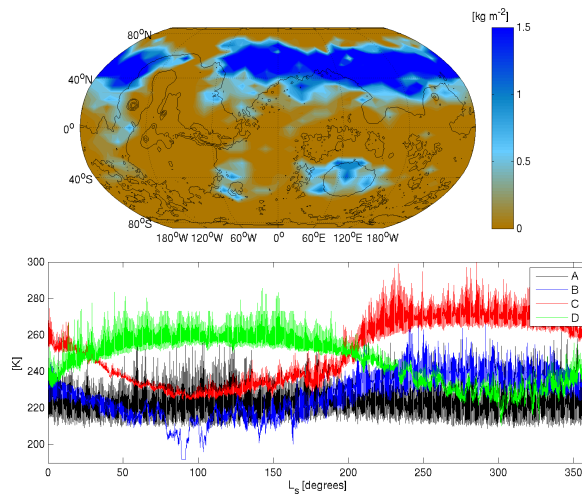


Fig. 12. (top) Maximum surface liquid water in one year after 40 years simulation time, for the 1-bar simulation with obliquity 25° shown in Figure 4. (bottom) Surface temperature vs. time for the same simulation, for the four locations displayed in Figure 15.

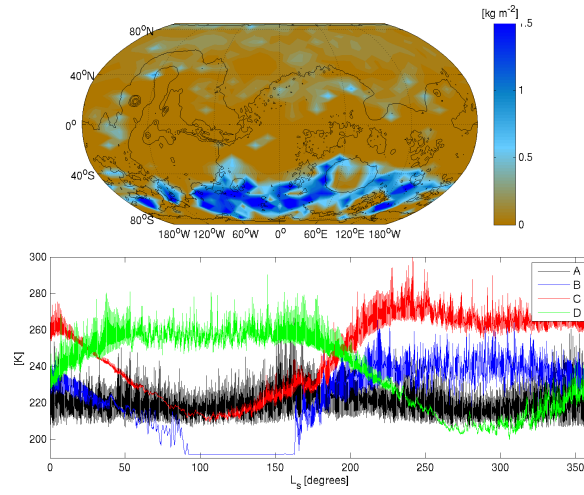


Fig. 13. Same as Figure 12, except for obliquity  $45^\circ$ .

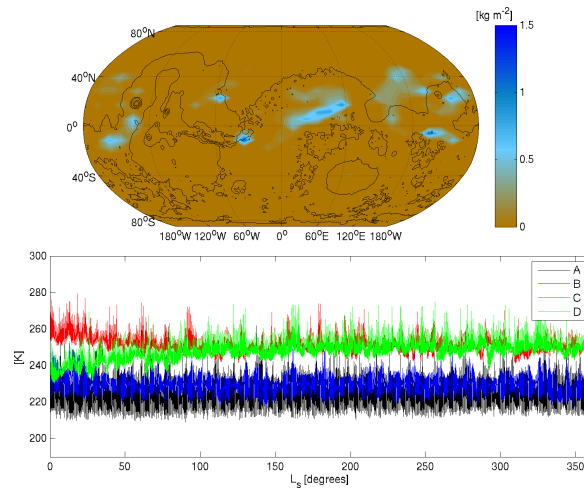


Fig. 14. Same as Figure 12, except with obliquity set to  $0^\circ$  after 40 years simulation time.

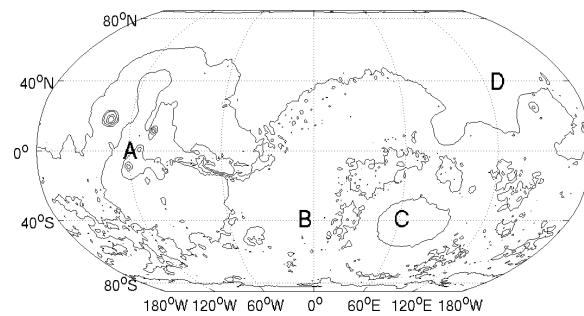


Fig. 15. Locations for the four temperature time series displayed in Figs. 12-14.

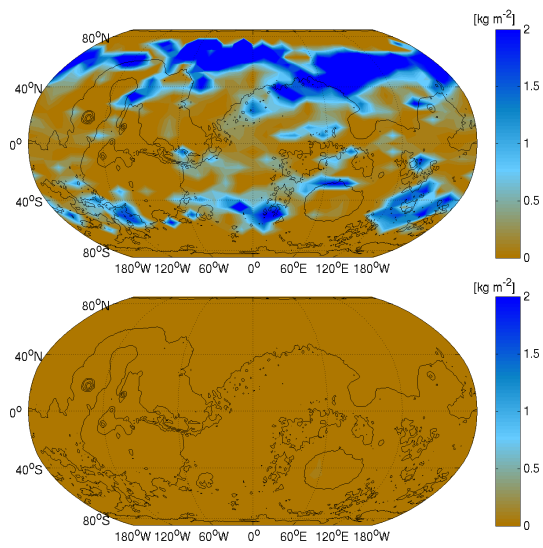


Fig. 16. Maximum surface liquid water in one year after 40 years simulation time, for the 1-bar simulation with obliquity  $25^\circ$  shown in Figure 4, after (left) change of ice surface albedo from 0.5 to 0.3 and (right) increase of ice surface thermal inertia from 250 to  $1000 \text{ J m}^{-2} \text{ s}^{-1/2} \text{ K}^{-1}$ .

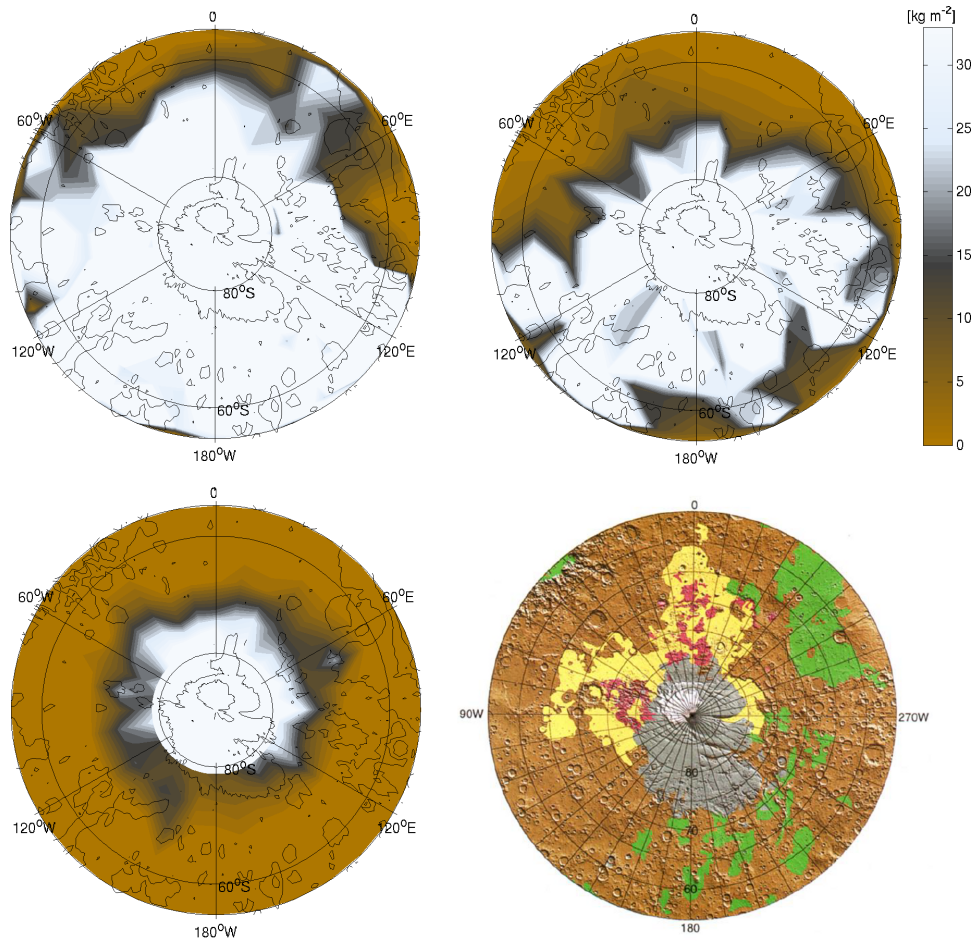


Fig. 17. Plots of the annual mean water ice coverage on the southern pole after 40 years for mean surface pressure 1 bar and obliquity a)  $25^\circ$ , b)  $45^\circ$  and mean surface pressure 0.2 bar and obliquity  $25^\circ$ . d) For comparison, a plot of the Dorsa Argentea Formation from Head and Pratt [2001] is also shown.

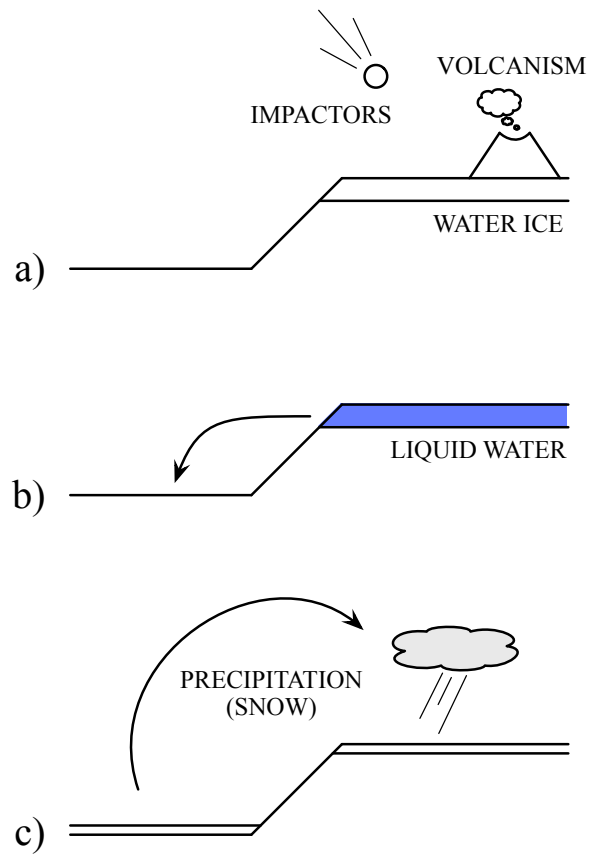


Fig. 18. Schematic of the effect of periodic melting events under a moderately dense  $\text{CO}_2$  atmosphere. a) In a steady state, ice deposits are concentrated in the colder highland regions of the planet. b) Impacts or volcanism cause transient ice melting and flow to lower lying regions on short timescales. c) On much longer timescales, ice is once again transported to highland regions via sublimation and light snowfall.